Astronomy & Astrophysics

The most luminous blue quasars at 3.0 < z < 3.3

III. LBT spectra and accretion parameters

Bartolomeo Trefoloni[1,2], Elisabeta Lusso[1,2], Emanuele Nardini[2], Guido Risaliti[1,2], Giada Bargiacchi[3,4], Susanna Bisogni[5], Francesca M. Civano[6], Martin Elvis[7], Giuseppina Fabbiano[7], Roberto Gilli[8], Alessandro Marconi[1,2], Gordon T. Richards[9], Andrea Sacchi[7,10], Francesco Salvestrini[2], Matilde Signorini[1,2], and Cristian Vignali[11,8]

[1] Dipartimento di Fisica e Astronomia, Università di Firenze, Via G. Sansone 1, 50019 Sesto Fiorentino, Firenze, Italy
e-mail: bartolomeo.trefoloni@unifi.it
[2] INAF – Osservatorio Astrofisico di Arcetri, Largo Enrico Fermi 5, 50125 Firenze, Italy
[3] Scuola Superiore Meridionale, Largo S. Marcellino 10, 80138 Napoli, Italy
[4] Istituto Nazionale di Fisica Nucleare (INFN), Sez. di Napoli, Complesso Univ. Monte S. Angelo, Via Cinthia 9, 80126 Napoli, Italy
[5] INAF – Istituto di Astrofisica Spaziale e Fisica Cosmica Milano, Via Corti 12, 20133 Milano, Italy
[6] NASA Goddard Space Flight Center, Code 660, Greenbelt, MD 20771, USA
[7] Center for Astrophysics | Harvard & Smithsonian, 60 Garden Street, Cambridge, MA 02138, USA
[8] INAF – Osservatorio di Astrofisica e Scienza dello Spazio di Bologna, Via Gobetti 93/3, 40129 Bologna, Italy
[9] Department of Physics, 32 S. 32nd Street, Drexel University, Philadelphia, PA 19104, USA
[10] Scuola Universitaria Superiore IUSS Pavia, Palazzo del Broletto, piazza della Vittoria 15, 27100 Pavia, Italy
[11] Dipartimento di Fisica e Astronomia, Università degli Studi di Bologna, Via Gobetti 93/2, 40129 Bologna, Italy

ABSTRACT

We present the analysis of the rest frame ultraviolet and optical spectra of 30 bright blue quasars at $z \sim 3$, selected to examine the suitability of active galactic nuclei as cosmological probes. In our previous works, based on pointed *XMM-Newton* observations, we found an unexpectedly high fraction ($\approx 25\%$) of X-ray weak quasars in the sample. The latter sources also display a flatter UV continuum and a broader and fainter C IV profile in the archival UV data with respect to their X-ray normal counterparts. Here we present new observations with the Large Binocular Telescope in both the *zJ* (covering the rest frame $\simeq 2300$–3100 Å) and the K_S ($\simeq 4750$–5350 Å) bands. We estimated black hole masses (M_{BH}) and Eddington ratios (λ_{Edd}) from the available rest frame optical and UV emission lines (Hβ, Mg II), finding that our $z \sim 3$ quasars are on average highly accreting ($\langle \lambda_{Edd} \rangle \simeq 1.2$ and $\langle M_{BH} \rangle \simeq 10^{9.7} M_\odot$), with no difference in λ_{Edd} or M_{BH} between X-ray weak and X-ray normal quasars. From the *zJ* spectra, we derived the properties (e.g. flux, equivalent width) of the main emission lines (Mg II, Fe II), finding that X-ray weak quasars display higher Fe II/Mg II ratios with respect to typical quasars. Fe II/Mg II ratios of X-ray normal quasars are instead consistent with other estimates up to $z \simeq 6.5$, corroborating the idea of already chemically mature broad line regions at early cosmic time. From the K_S spectra, we find that all the X-ray weak quasars present generally weaker [O III] emission (EW < 10 Å) than the normal ones. The sample as a whole, however, abides by the known X-ray-[O III] luminosity correlation, hence the different [O III] properties are likely due to an intrinsically weaker [O III] emission in X-ray weak objects, associated to the shape of the spectral energy distribution. We interpret these results in the framework of accretion-disc winds.

Key words. galaxies: active – quasars: general – quasars: supermassive black holes – quasars: emission lines – accretion, accretion disks

1. Introduction

Quasars are the most luminous persistent sources in the Universe, and as such they represent a class of objects of fundamental importance to understanding the mechanisms of production of radiation and the interplay with gas and dust up to very high redshift. Quasars belong to the high–luminosity tail ($L_{bol} > 10^{45}$ erg s^{-1}) of the active galactic nuclei (AGN) population and, according to the current paradigm, their emission is powered by accretion onto a supermassive black hole (SMBH) with mass (M_{BH}) > $10^6 M_\odot$. The main contribution to their broadband spectral energy distribution (SED) comes from the optical and UV emission produced by the disc (e.g. Salpeter

1964; Lynden-Bell 1969; Czerny & Elvis 1987) and X-ray emission from the so-called corona (e.g. Sunyaev & Titarchuk 1980; Haardt & Maraschi 1993), where the energy of the UV seed photons emitted by the disc is boosted via inverse-Compton scattering. The UV emission is accompanied by a shallow bump in the infrared (due to dust reprocessing in the torus), whilst strong radio emission, if present, is generally linked to a jet.

The high luminosity observed in quasars, as well as the growing number of available observations up to high redshift (e.g. Mortlock et al. 2011; Bañados et al. 2018; Yang et al. 2020, but see also Kroupa et al. 2020 for an alternative explanation), make them valuable objects to investigate the cosmological parameters, as proposed by our group (e.g. Risaliti & Lusso 2015)

by making use of the non-linear relation between their UV and X-ray luminosity (the $L_X - L_{UV}$ or, equivalently, the $\alpha_{OX} - L_{UV}$ relation[1]: e.g. Avni & Tananbaum 1986). Such a relation was found to be independent of redshift (e.g. Vignali et al. 2003; Steffen et al. 2006; Green et al. 2009; Lusso & Risaliti 2016); however, the interplay between corona and disc could in principle vary with the bolometric luminosity (L_{bol}) and/or the Eddington ratio (λ_{Edd}), defined as L_{bol}/L_{Edd}, where L_{Edd} is the Eddington luminosity. At high λ_{Edd}, for instance, the framework of a geometrically thin and optically thick disc (Shakura & Sunyaev 1973) could break down, as the disc is expected to thicken (Abramowicz et al. 1988; Chen & Wang 2004; Wang et al. 2014), a behaviour also shown by simulations (Ohsuga & Mineshige 2011; Jiang et al. 2014, 2016, 2019; Sądowski et al. 2014). Moreover, perturbations to the standard accretion process could be associated with the presence of powerful accretion-disc winds, directly driven by the nuclear activity (e.g. Proga 2005). Highly efficient accretion is an ideal condition for the launch of such outflows (Zubovas & King 2013; Nardini et al. 2015, 2019a; King & Pounds 2015), which could justify the observed relations between the SMBH mass and the galaxy properties (e.g. the $M_{BH} - \sigma$ relation; Ferrarese & Merritt 2000; Gebhardt et al. 2000; Marconi & Hunt 2003; King 2005), although it is not yet clear whether and how AGN-driven outflows can affect their host galaxies.

Remarkably, at high λ_{Edd} several quasar samples sharing similar UV properties have recently shown an enhanced fraction of objects ($\approx 25\%$) whose X-ray spectra are relatively flat ($\langle \Gamma \rangle \simeq 1.6$) and underluminous (by factors of $>3-10$) with respect to what is expected according to the $L_X - L_{UV}$ relation (e.g. Luo et al. 2015; Nardini et al. 2019b; Zappacosta et al. 2020; Laurenti et al. 2022), in many cases without any clear evidence for absorption as revealed by the spectral analysis.

A high λ_{Edd} is also conducive to a higher prominence of the Fe II emission line complex (e.g. Boroson & Green 1992; Marziani et al. 2001; Zamfir et al. 2010; Shen & Ho 2014). This feature, in turn, can be employed to investigate the chemical enrichment of the broad-line region (BLR) of quasars through the Fe II/Mg II ratio up to very high redshift ($z \lesssim 7$). The Fe II/Mg II ratio seems to correlate with λ_{Edd} and M_{BH}, but does not show any clear trend with the AGN luminosity (e.g. Dong et al. 2011; Shin et al. 2019, 2021). Despite numerous studies (e.g. Kawara et al. 1996; Thompson et al. 1999; Iwamuro et al. 2002, 2004; Dietrich et al. 2003; Barth et al. 2003; Freudling et al. 2003; Maiolino et al. 2003; Tsuzuki et al. 2006; Jiang et al. 2007; Kurk et al. 2007; Sameshima et al. 2009, 2020; De Rosa et al. 2011, 2014; Mazzucchelli et al. 2017; Shin et al. 2019), it is still unclear whether any evolutionary trend of this ratio exists, also because of the large uncertainties on the measurements of this quantity.

This paper is the third dedicated to the analysis of the spectral properties of 30 luminous quasars ($L_{bol} > 8 \times 10^{46}$ erg s^{-1}) at redshift $z = 3.0-3.3$ (Nardini et al. 2019b, Paper I). Here, we focus on the Mg II $\lambda 2798$ emission line probed by dedicated observations at the Large Binocular Telescope (LBT) in the zJ band, and on the Hβ–[O III] complex for a subsample observed in the K_S band. Our main aim is to investigate whether any evidence of a difference in the optical-UV properties (e.g. emission line strengths, continuum) exists between X-ray normal and X-ray weak quasars.

Throughout the paper we refer to X-ray normal quasars as the N group, and to X-ray weak quasars and weak candidates as the $W+w$ group (i.e. we do not distinguish between X-ray weak, W, and weak candidates, w). For the operational definition of X-ray normal (N), weak (W) and weak candidates (w), we refer the interested reader to Sect. 2.3 of Lusso et al. (2021, Paper II). The paper is structured as follows: the quasar sample and the observations are described in Sect. 2, whilst the analysis of UV and optical spectra is reported in Sect. 3. Results are presented and discussed in Sects. 4 and 5, and conclusions are drawn in Sect. 6.

2. Observations and data reduction

2.1. The data set

The quasar sample analysed here consists of 30 luminous quasars ($L_{bol} > 10^{46.9}$ erg s^{-1}) at $z \sim 3$, for which X-ray observations were obtained through an extensive campaign performed with *XMM-Newton*. This sample, selected in the optical from the Sloan Digital Sky Survey (SDSS) Data Release 7 (Abazajian et al. 2009) as representative of the most luminous, intrinsically blue radio-quiet quasars, boasts by construction a remarkable degree of homogeneity in terms of optical-UV properties. The reader can find more details on the sample selection in the Supplementary Material of Risaliti & Lusso (2019; see also Lusso et al. 2020 for a more general discussion of the selection criteria employed to define homogeneous samples of quasars in the optical-UV). While we refer the reader interested in the X-ray analysis to Paper I, we briefly summarise the main results below.

About two-thirds of the sample show X-ray luminosities in agreement with the values expected from the $L_X - L_{UV}$ relation, and an average continuum photon index of $\Gamma_X \sim 1.85$, fully consistent with AGN at lower redshift, luminosity, and M_{BH} (e.g. Just et al. 2007; Piconcelli et al. 2005; Bianchi et al. 2009b). Their 2–10 keV band luminosities are in the range $4.5 \times 10^{44} \leq L_{2-10 keV} \leq 7.2 \times 10^{45}$ erg s^{-1}, representing one of the most X-ray luminous samples of radio-quiet quasars ever observed. Conversely, one-third of the sources are found to be underluminous by factors of $\gtrsim 3-10$. X-ray absorption at the source redshift is not statistically required in general by the fits of the X-ray spectra and, despite the poor quality of the data in a handful of cases that does not allow us to definitely exclude some absorption, column densities $N_H(z) > 3 \times 10^{22}$ cm^{-2} can be confidently ruled out.

In Paper II we analysed the C IV $\lambda 1549$ emission line properties (e.g. equivalent width, EW; line peak velocity, v_{peak}) and UV continuum slope as a function of the X-ray photon index and 2–10 keV flux. In summary, we found that the composite spectrum of X-ray weak quasars is flatter ($\alpha_\lambda \sim -0.6$) than that of X-ray normal quasars ($\alpha_\lambda \sim -1.5$). The C IV emission line is on average fainter in the X-ray weak sample, but only a modest blueshift (600–800 km s^{-1}) is reported for the C IV lines of both stacks. This emission feature is found to be broader in the $W+w$ stacked spectrum where it exhibits a higher full width at half maximum ($FWHM \simeq 10\,000$ km s^{-1}) than in the N spectrum ($\simeq 7000$ km s^{-1}), but still in agreement with previous results on the topic at similar redshifts (e.g. Richards et al. 2002; Shen et al. 2011) and luminosities (e.g. Vietri et al. 2018). When we added the sample from Timlin et al. (2020; filtered out according to our selection criteria) in order to expand the dynamical range of the parameters of interest, we were able to confirm the statistically significant trends of C IV v_{peak} and EW with

---

[1] α_{OX} is defined as a function of the monochromatic flux densities at rest frame 2500 Å and 2 keV as $\alpha_{OX} = 0.384 \, \text{Log}(F_{2 keV}/F_{2500 Å})$.

Table 1. Log of the LUCI/LBT zJ observations.

Name	Obs. date [a]	t_{exp} [b]	S/N [c]	Seeing [d]	Instr. [e]
J0301−0035	2019 Sep. 28	1320	49	1.0	LUCI1
J0304−0008	2019 Sep. 28	1680	43	1.0	LUCI1
J0826+3148	2019 Oct. 17	1920	28	1.0	LUCI1
J0835+2122	2019 Oct. 17	1680	35	1.1	LUCI1
J0900+4215	2020 Feb. 02	480	22	1.2	LUCI2
J0901+3549	2020 Feb. 02	1200	24	0.8	LUCI2
J0905+3057	2020 Feb. 03	1680	27	1.1	LUCI2
J0942+0422	2020 Nov. 12	960	24	1.2	LUCI1+LUCI2
J0945+2305	2020 Dec. 26	6000	37	1.0	LUCI1+LUCI2
J0947+1421	2020 Dec. 26	840	33	0.9	LUCI1+LUCI2
J1014+4300	2020 Dec. 26	720	46	0.8	LUCI1+LUCI2
J1027+3543	2020 Dec. 26	840	17	0.8	LUCI1+LUCI2
J1111−1505	2021 Apr. 02	2700	26	0.9	LUCI1+LUCI2
J1111+2437	2021 Jan. 09	3360	33	1.4	LUCI1+LUCI2
J1143+3452	2021 Jan. 12	2160	33	1.0	LUCI1+LUCI2
J1148+2313	2021 Jan. 17	1440	23	0.8	LUCI1+LUCI2
J1159+3134	2021 Jan. 17	1800	18	0.9	LUCI1+LUCI2
J1201+0116	2021 Apr. 02	960	35	0.9	LUCI1+LUCI2
J1220+4549	2021 Jan. 31	1500	35	0.8	LUCI1+LUCI2
J1225+4831	2021 Feb. 01	1920	18	0.7	LUCI1+LUCI2
J1246+2625	2020 Jun. 23	1200	25	0.7	LUCI2
J1246+1113	2020 Jun. 23	2400	15	0.8	LUCI2
J1407+6454	2020 Jun. 23	1080	30	0.8	LUCI2
J1425+5406	2020 Jun. 26	1050	29	0.9	LUCI2
J1426+6025	2020 Jun. 27	300	15	0.8	LUCI2
J1459+0024	2020 Jun. 27	1650	12	0.9	LUCI2
J1532+3700	2020 Jun. 26	900	21	0.9	LUCI2
J1712+5755	2019 Oct. 19	960	12	1.1	LUCI1
J2234+0000	2019 Sep. 28	1350	16	0.9	LUCI1+LUCI2

Notes. [a]Observation Date. [b]Total exposure. [c]Signal-to-noise ratio in the observed wavelength range 1.05–1.10 μm. [d]Average seeing of the observation in arcseconds. [e]LUCI camera used for the observation.

UV luminosity at 2500 Å for both X-ray weak and X-ray normal quasars, as well as the correlation between X-ray weakness and the EW of C IV. However, we did not observe any clear relation between the 2–10 keV luminosity and v_{peak}. We found a statistically significant correlation between the hard X-ray flux and the integrated C IV flux for X-ray normal quasars, which extends across more than three (two) decades in C IV (X-ray) luminosity, whilst X-ray weak quasars deviate from the main trend by more than 0.5 dex.

To interpret these results, we argued that X-ray weakness might arise in a starved X-ray corona picture, possibly associated with an ongoing disc-wind phase. If the wind is ejected in the vicinity of the black hole, the accretion rate across the final gravitational radii will diminish, so depriving a compact, centrally confined corona of seed UV photons and resulting in an X-ray weak quasar. However, at the largest UV luminosities ($>10^{47}$ erg s^{-1}), there will still be sufficient ionising photons that can explain the 'excess' C IV emission observed in the X-ray weak quasars with respect to normal sources of similar X-ray luminosities (see Fig. 14 in Paper II).

2.2. LUCI/LBT observations

In addition to the effects on the C IV emission line, we are interested in assessing whether the dearth of X-ray photons could affect other emission lines, such as the [O III] $\lambda\lambda4959, 5007$ Å doublet, whose production needs at least $\simeq35$ eV ($\simeq354$ Å)

photons, and the Hβ line. Moreover, wavelengths longer than 2200 Å, not covered by the SDSS spectra in this redshift interval, are key to determining the continuum fluxes at rest frame 2500 Å and to inspecting the UV Fe II and Fe III emission often included among the characteristic parameters of X-ray weak quasars (e.g. Leighly et al. 2007a; Marziani & Sulentic 2014; Luo et al. 2015). Therefore, observations of this spectral interval are important for several reasons. For instance, the analysis of the Mg II emission line provides generally more reliable estimates of BH masses than the C IV-based estimates, to test whether any systematic difference between the BH masses and Eddington ratios of the X-ray weak and normal quasars is present. Additionally, we can estimate the Fe II/Mg II ratio in our sample, which represents a proxy of the gas metallicity at redshift $z \sim 3$.

To investigate these issues, our group was awarded observing time with the two LBT Utility Cameras in the Infrared (LUCI1 and LUCI2; Ageorges et al. 2010) at the 8.4 m Large Binocular Telescope (LBT) located on Mount Graham (Arizona), to carry out near-infrared spectroscopy of the $z \sim 3$ quasars in the zJ and K_S bands. LUCI observations were performed between November 2018 and April 2021 with the zJ filter coupled with grism G200 and the K_S filter coupled with grism G150, covering an observed range of 0.9–1.2 μm and 1.95–2.40 μm, respectively. A slit width of 1″ was employed, providing a spectral resolution $R = 1050$–1200 in zJ and 2075 in K_S. The journal of the observations is shown in Tables 1 and 2, where we list the seeing

Table 2. Log of the LUCI1/LBT K_S observations.

Name	Obs. date [a]	$t_{\rm exp}$ [b]	S/N [c]	Seeing [d]
J0303−0023	2018 Nov. 06	2400	25	0.9
J0304−0008	2018 Nov. 07	2420	15	1.0
J0945+2305	2018 Nov. 08–09	4960	18	0.7
J0942+0422	2018 Nov. 11	1650	38	1.0
J1220+4549	2019 Jan. 26	2875	10	1.0
J1111+2437	2019 Jan. 26	2645	21	1.0
J1201+0116	2019 Jan. 28	800	29	1.7
J1425+5406	2019 Feb. 28	2415	42	0.8
J1426+6025	2019 Apr. 27	600	51	1.0

Notes. [a]Observation date. [b]Total exposure. [c]Signal-to-noise ratio in the observed wavelength range 2.04–2.20 μm. [d]Average seeing of the observation in arcseconds.

measured during the observations and the average signal-to-noise ratio (S/N) in the observed wavelength ranges 1.05–1.10 μm and 2.04–2.20 μm of the final flux-calibrated spectra.

Observations in the zJ band were performed for all the quasars but one (J1507+2419), which was too faint to be observed with an exposure time comparable with the rest of the sample. Regarding the K_S observations, a further constraint on the redshift ($z = 3.19-3.29$) within the sample was dictated by the requirement that the [O III] emission line falls in a wavelength range (2.10−2.15 μm) with good atmospheric transmission. This condition allowed us to observe only nine targets, for which the K_S spectroscopic data[2] were acquired from November 2018 to April 2019 with seeing of around $0.7''-1.0''$.

The 2D raw spectra were reduced by the LBT Spectroscopic Reduction Center at INAF – IASF Milano, with a reduction pipeline optimised for LBT data (Scodeggio et al. 2005; Gargiulo et al. 2022) performing the following steps. For each source, calibration frames are created for both LUCI1 and LUCI2. Imaging flats and darks are used to create a bad pixel map, applied to every single observed frame, along with a correction for cosmic rays. Dark and flat-field corrections are applied independently to each observed frame through a master dark and a master flat, obtained from a set of darks and spectroscopic flats. A master lamp describes the inverse solution of the dispersion to be applied to individual frames to calibrate in wavelength and remove any curvature due to optical distortions. The mean accuracy achieved for the wavelength calibration is 0.26 Å in the K_S band and 0.22 Å (0.25 Å) for LUCI1 (LUCI2) in the zJ band. The 2D wavelength-calibrated spectra are then sky-subtracted following the method described in Davies (2007). The flux calibration is then applied to the 2D spectra through the sensitivity function, obtained from the spectrum of a star observed close in time and air-mass to the scientific target. Finally, wavelength- and flux-calibrated, sky-subtracted spectra are stacked together, and the 1D spectrum of the source is extracted. We checked the zJ (K_S) flux calibration by convolving each spectrum with the 2MASS J (K_S) filter to compute its J- (K_S-) band Vega magnitude, and then corrected to match to the observed value reported by SDSS DR16v4 (Ahumada et al. 2020). The uncertainty on the flux-calibrated spectrum was estimated as the squared sum of a statistic term given by the mean rms of left and right telescopes and a calibration factor $\Delta m/m = (m_{\rm LBT} - m_{\rm 2MASS})/m_{\rm 2MASS}$.

There is no overlapping region between the LBT zJ and the SDSS spectra, which leaves a small gap between them. Since

the two segments of each spectrum were not collected simultaneously, part of the observed flux gap can be due to some intrinsic variation of the emission, but we expect this contribution to be rather small since more luminous quasars tend to be less variable in time (e.g. Uomoto et al. 1976; Cristiani et al. 1996; Wilhite et al. 2008). Systematics in the flux calibration could also be involved, but in principle their contribution should be small since SDSS spectrophotometric calibration is accurate to 4% rms for point sources (Adelman-McCarthy 2008). LBT flux recalibration factors with respect to the 2MASS J (K_S) filter are in the range 0.6−1.9 (0.4−1.7) with a mean value of 1.02 (0.93).

3. Analysis

3.1. Fitting procedure

The spectral fits of the zJ and K_S data were both performed through a custom-made code, based on the IDL MPFIT package (Markwardt 2009), which takes advantage of the Levenberg–Marquardt technique (Moré 1978) to solve the least-squares problem.

The region roughly between 2400 Å and 3200 Å corresponding to the rest frame of the zJ spectra is mainly characterised by Fe II and Fe III emission lines (which blend in a pseudo-continuum), the Balmer continuum, and the Mg II 2798 Å emission line. In this region there are only two small continuum windows between 2650–2670 Å and 3030–3070 Å (Mejía-Restrepo et al. 2016), but the former was often included in the atmospheric absorption band that affects the range ~1.11–1.16 μm in the observed frame. This, together with the lack of other bright emission lines and/or other continuum windows, led to the problem of having only one narrow interval to anchor the power-law continuum, thus leading to a degeneracy between the slope of the power law and the strength of iron emission.

In order to break this degeneracy, we followed a similar approach to that described in Vietri et al. (2018). Thus, we adopted the same value of the continuum power-law slope as derived from the SDSS spectra in Paper II for each source. In the six cases where multiple SDSS observations were available (J0303–0023, J0303–0008, J111–1505, J1159+3134, J1407+6454, J1459+0024), we assumed the average of the individual best-fit spectral indices. We then accounted for the remaining emission with the required number of Fe II templates, as produced by different synthetic photoionisation models through the CLOUDY simulation code (Ferland et al. 2013), and convolved with different Gaussian profiles with a velocity dispersion of up to 7000 km s^{-1}. Broad Gaussian components
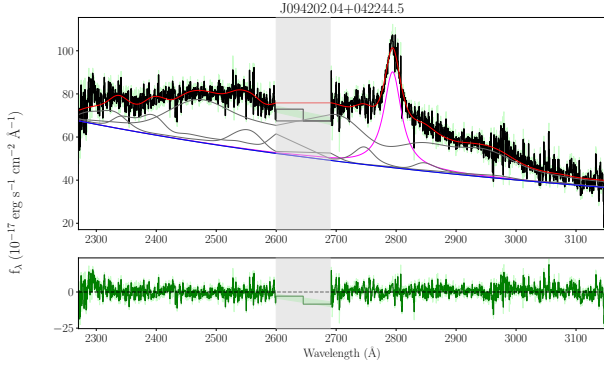
---

[2] K_S observations were performed with LUCI1 only.

Fig. 1. Example of LBT zJ spectral fit. Top panel: Spectrum (black), global model (red), and model components of a typical LBT zJ fit (J0942+0422). The continuum power law is shown in blue, the Mg II line in magenta, the iron pseudo-continuum in dark grey. The shaded light grey band corresponds to the observed-frame atmospheric absorption window at 1.11–$1.16\,\mu$m and is not included in the fit. Bottom panel: Global model residuals (green).
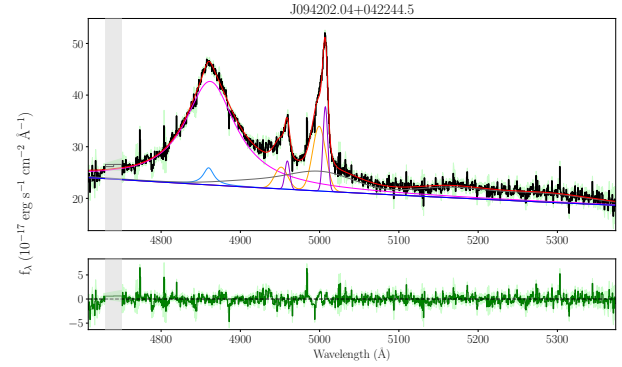

Fig. 2. Example of LBT K_S spectral fit. Top panel: Spectrum (black), global model (red), and model components of a typical LBT K_S fit (J0942+0422). The continuum power law is shown in blue, the broad and narrow Hβ in magenta and turquoise, the [O III] doublet in orange and violet, and the iron pseudo-continuum in dark grey. The shaded light grey band is affected by poor atmospheric transmission and is not included in the fit. Bottom panel: Global model residuals (green).

($FWHM > 1000\,{\rm km\,s}^{-1}$) were added in some cases, to provide a more faithful description of the iron profile. This procedure gave satisfactory results for most of the spectra (see Appendix A). Furthermore, in Appendix C we report on checking the reliability of fixing the power-law slope in order to match that of the continuum underlying the C IV line and the continuum windows at bluer wavelengths, and we compared our way of estimating the strength of Fe II with that in the archival data.

The model adopted to fit the K_S spectra included a multi-Gaussian (one broad, one or two narrow) deconvolution for the emission lines (i.e. Hβ $\lambda 4861$ and [O III] $\lambda\lambda 4959, 5007$), and Fe II templates to account for the optical iron emission. The ratio of the core [O III] $\lambda 4959$ to $\lambda 5007$ components was fixed at one to three, and a blue component for both [O III] lines was also included to account for possible outflows from the narrow-line region (NLR). Examples of the fits performed on typical LBT zJ- and K_S-band spectra are shown, respectively, in Figs. 1 and 2.

3.2. Composite spectra

To build the composite LBT spectra for the X-ray weak and X-ray normal quasars, we followed a similar procedure to the one described in Lusso et al. (2015). For the sake of consistency with the assumptions made in Paper II, we excluded from the stack the radio-bright (J0900+4215), the two broad absorption line quasars (BAL) (J0945+2305, J1148+2313), and the reddest (J1459+0024) quasars. As the last three are X-ray weak, we wanted to avoid an enhanced flatness of the resulting composite spectrum as a result of their BAL–red nature. This further selection brought the X-ray weak group of LBT zJ (K_S) spectra down to seven (four) objects. In particular, to build the composite spectra we took the following steps:

1. We corrected the quasar flux density[3] f_λ for Galactic reddening by adopting the $E(B-V)$ estimates from Schlegel et al. (1998) and the Galactic extinction curve from Fitzpatrick (1999) with $R_V = 3.1$.
2. We generated a rest frame wavelength array with fixed dispersion for the zJ (K_S) spectra with $\Delta\lambda$ equal to 2.25 Å (2.39 Å), roughly corresponding to the resolution at the central wavelength of the observed spectra ($R = 1125$ at

1.05 μm and $R = 2075$ at 2.105 μm, respectively, for zJ and K_S), shifted to the rest frame according to the mean quasar redshift.
3. We shifted each quasar spectrum to the rest frame and linearly interpolated over the rest frame wavelength array with fixed dispersion $\Delta\lambda$, while conserving its flux.
4. We normalised every spectrum by their integrated flux over the wavelength ranges 2400–3100 Å (zJ) and 4800–5300 Å (K_S), which are covered by all the spectra.
5. We extracted the median value of the normalised fluxes in each spectral channel. The uncertainty on the median flux in a spectral channel was estimated as the 95% semi-interquartile range of the fluxes divided by the square root of the number of spectra in that channel.

The spectral stacks obtained with the procedure described above are shown in Figs. 3 and 4 for the zJ and the K_S data, respectively. As a reference, we also overplot the average quasar spectrum from Vanden Berk (2001), which is built from 2204 SDSS spectra spanning a redshift range $0.044 \le z \le 4.789$. If we extrapolate the slope of the continuum found in Paper II to the wavelengths covered by the LBT spectra, the flatter continuum in the X-ray weak composite hints at a larger EW of Fe II compounds, as also suggested by the analysis of the individual sources. We discuss this point further in Sect. 4. Despite the emission line differences, the two composites are in broad agreement with the reference spectrum, thus implying no strong evolution of the general spectral properties of the $z \sim 3$ sample with respect to AGN at other redshifts.

3.3. Black hole masses and Eddington ratios

We computed single-epoch $M_{\rm BH}$ from the available emission lines with known reliable virial relations for each object. In the SDSS spectra, the C IV $\lambda 1549$ line is available for the whole sample, whereas the Mg II $\lambda 2798$ line, present in all the LBT zJ spectra, in 18/29 cases is fully or marginally hidden by atmospheric absorption, hindering a reliable determination of its FWHM. Hβ was used for the nine objects in the LBT K_S subsample. It is well known that BH masses from different lines have a different reliability: Hβ-based masses are generally regarded as the benchmark (see e.g. Denney 2012; Shen 2013; Dalla Bontà et al. 2020), but in this case they are only available for a minority of sources.
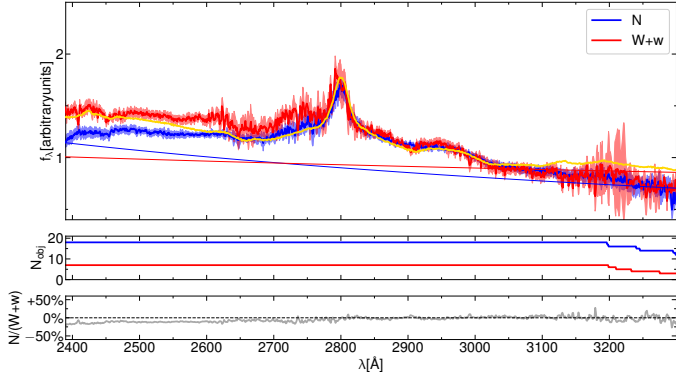
---

[3]   In the following, we use the word 'flux' to mean the flux density (i.e. flux per unit wavelength) unless specified otherwise.

Fig. 3. Composite LBT *zJ* spectra for *N* and *W* + *w* quasars. Top panel: Median LBT *zJ* spectra for the X-ray normal (*N*, in blue) and the X-ray weak (*W+w*, in red) subsamples. The gold spectrum is the average quasar spectrum from Vanden Berk (2001). Fluxes are normalised by their value at 3000 Å. The continuum power laws are the extrapolation of those found at UV wavelengths (i.e. SDSS). Middle panel: Number of spectra contributing to each spectral channel, following to the same colour-coding. Bottom panel: Ratio of the *N* spectrum to the *W+w* spectrum.
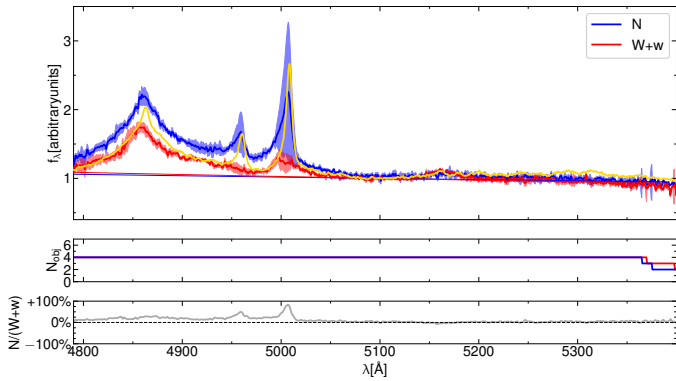
Fig. 4. Composite LBT K_S spectra for *N* and *W* + *w* quasars. Top panel: Median LBT K_S spectra for the X-ray normal and the X-ray weak subsamples. The colour-coding is the same as in Fig. 3. Fluxes are normalised by their value at 5100 Å. Middle panel: Number of spectra contributing to each spectral channel, following the same colour-coding. Bottom panel: Ratio of the *N* spectrum to the *W+w* spectrum.

Mg II-based masses are consistent, within their non-negligible systematic uncertainty (~0.3 dex; Shen et al. 2011), with the Hβ values. On the other hand, while C IV-based masses only provide a very rough estimate of the mass of the black hole powering the AGN, this emission feature is present for every object in the sample, and in 18/29 objects this is the only available tool to estimate the BH mass. The inclusion of C IV-based BH masses comes with two caveats. First, the C IV emission line centroid can show blueshifts up to about 10 000 km s^{-1} with respect to the systemic redshift, suggesting the presence of an outflowing phase (Baskin & Laor 2005a; Richards et al. 2006), not compatible with the virial assumption under which BH masses are estimated. This can cause an overestimate of the BH mass by up to an order of magnitude (e.g. Kratzer & Richards 2015). Second, C IV calibrations should be considered with caution since they are affected by significant scatter due to different systematics, eventually allowing us to derive BH masses only at the price of large uncertainties, ≳0.4 dex (Shen et al. 2011; Shen & Liu 2012; Rakshit et al. 2020; Wu & Shen 2022). To mitigate these

issues, BH masses based on the C IV FWHM were estimated by adopting the corrections described in Coatman et al. (2017), suitable for objects with a blueshifted C IV emission. We employed the offset velocities reported in Paper II to perform the correction of the FWHM and subsequently of M_{BH} for objects whose blueshifts are positive, whereas the correction factors were set to unity otherwise (3/29 objects) since the authors themselves cautioned against using their correction in case of negative blueshift (i.e. redshift) of the C IV line centroid.

We estimated single-epoch masses based on the continuum luminosity (λL_λ) evaluated close to the considered emission line and its FWHM through the expression

$$\mathrm{Log}\left(\frac{M_{BH}}{M_\odot}\right) = A + B\,\mathrm{Log}\left(\frac{\lambda L_\lambda}{10^{44}\mathrm{erg\,s}^{-1}}\right) + 2\,\mathrm{Log}\left(\frac{FWHM}{\mathrm{km\,s}^{-1}}\right),\quad (1)$$

where the *A* and *B* coefficients were calibrated by different authors for each line as

$$(A, B) = \begin{cases} (0.71, 0.53) & \text{C IV } 1549\,\text{Å} & \text{Coatman et al. (2017)} \\ (0.74, 0.62) & \text{Mg II } 2798\,\text{Å} & \text{Shen et al. (2011)} \\ (0.70, 0.50) & \text{Hβ} & \text{Bongiorno et al. (2014).} \end{cases}$$
$$(2)$$

The wavelengths 1350 Å, 3000 Å, and 5100 Å were adopted to estimate the continuum luminosity for the C IV, Mg II, and Hβ emission lines, respectively. The data availability from the UV to the visible for nine objects allowed us to verify the reliability of the calibrations by comparing pairs of BH mass estimates. SMBH masses from the C IV line were compared to those already estimated in Wu & Shen (2022). To this end, we computed the distribution of the differences $\Delta\mathrm{Log}(M_{BH}) = \mathrm{Log}(M_{BH,CIV}) - \mathrm{Log}(M_{BH,SDSS})$. The mean value and the standard deviation of this distribution are $\langle\Delta\mathrm{Log}(M_{BH})\rangle = -0.05$ and $\sigma_{\Delta\mathrm{Log}(M_{BH})} = 0.3$. The minor offset of the distribution could be due to the prescription for the evaluation of the BH mass (in Wu & Shen 2022 the authors adopted the calibration from Vestergaard & Peterson 2006) and/or to the fitting procedure, but in general we do not find strong outliers.

For all the objects whose spectra included the Hβ emission line, the Mg II λ2798 line and the 3000 Å luminosity were also available; therefore it was possible to provide an additional estimate of the BH masses and compare them with the Hβ-based values. C IV- and Mg II-based BH masses against Hβ-based masses are shown in Fig. 5. The uncertainty is dominated by the systematic term (0.4 dex for C IV and 0.3 dex for Mg II and Hβ-based masses), being the statistical uncertainty on the BH masses on average 17% for the C IV, 5% for the Hβ, and 2% for the Mg II estimates. The fiducial mass for each object was derived as a weighted mean, using as weight the total uncertainty on each mass estimate, given by the square root of the squared sum of the systematic term and the statistical term. BH masses are listed in Table A.1 together with the best-fit line and continuum parameters.

Eddington ratios ($\lambda_{Edd} = L_{bol}/L_{Edd}$) were calculated by assuming the standard definition of $L_{Edd} = 1.26 \times 10^{38}\,(M_{BH}/M_\odot)\,\mathrm{erg\,s}^{-1}$. The L_{bol} value was computed for each object as stated in Paper I, by employing the 1350 Å monochromatic luminosity available from SDSS photometry and the bolometric correction of Richards et al. (2006). Considering the uncertainties on the BH masses, and the uncertainties on the bolometric conversion factors, which in the case of the 1350 Å luminosity can be up to 50% (Richards et al. 2006), we can only give crude estimates of the Eddington ratios. We found that, on
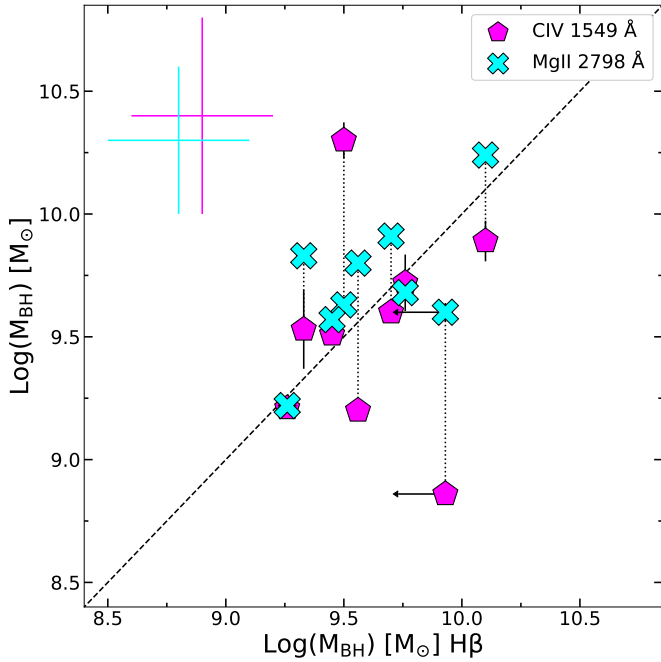
Fig. 5. Single-epoch M_{BH} comparison. The estimates based on C IV $\lambda1549$ (magenta pentagons) and Mg II $\lambda2798$ (cyan crosses) are shown against the broad Hβ $\lambda4861$ values. The typical systematic uncertainty of the calibrations is shown in the top left corner with the same colour-coding, while the dashed black line represents the 1:1 relation. The dotted lines join BH mass estimates for the same object according to different emission lines. The Hβ BH mass for J1111+2437 is denoted as an upper limit since the line profile is not well defined (see Appendix E for details).

average, our sources are close to the Eddington limit, with a median λ_{Edd} of 0.9, which is expected given the very high luminosities observed in the $z \sim 3$ sample.

4. Results

4.1. Mg II and Fe II emission

Intense Fe II emission and high Fe II/Mg II ratios are typically observed for X-ray weak sources (e.g. PHL 1811; Leighly et al. 2007a). We thus estimated the rest frame equivalent width for both the Mg II line and the Fe II emission complex to assess whether possible differences arise between the X-ray weak and X-ray normal quasars in our sample. However, the significance[4] of any difference between the two samples is limited by the small statistics (18 N vs 10 $W+w$ objects, excluding the radio bright J0900+4215 in the LBT zJ, and 4 N vs 5 $W+w$ objects in the LBT K_S spectral samples).

We found that the mean value of EW Mg II with the standard error of the mean for the N group is $\langle$EW Mg II$\rangle_N = 59 \pm 9$ Å, while $\langle$EW Mg II$\rangle_{W+w} = 66 \pm 13$ Å for the $W+w$ group, without any statistically significant difference between the two samples. However, potential differences could be diluted by the blend of Mg II with the Fe emission. In this analysis, we considered all the Mg II lines for which the full profile was available, including BAL quasar J0945+2305 (the other BAL and the reddest object

did not show an analysable Mg II profile). However, the results do not change if we exclude the latter source.

The mean EW Fe II of the N sample is $\langle$EW Fe II $\rangle_N = 292 \pm 40$ Å, which is somewhat smaller than the value obtained for the $W+w$ sample, $\langle$EW Fe II$\rangle_{W+w} = 469 \pm 70$ Å. The difference is statistically significant at the 2.2σ level, and a Kolmogorov–Smirnov (KS) test provides a p-value $= 0.017$, implying that the two distributions are indeed different at the 98.3% level. In the estimate of Fe II mean values we neglected the source J1225+4831, whose power-law continuum as extrapolated from the SDSS spectrum is significantly steeper than that required to adequately fit the Mg II emission line (see Appendix E for details). Even attempting a free-slope fit, there is a very faint Fe II contribution.

Both EW Fe II and EW Mg II were estimated by normalising the integrated flux of the line by the continuum flux at 3000 Å, as generally done for such ratios (e.g. Sameshima et al. 2020). The ratio of the equivalent widths of Fe II to Mg II shows, on average, a higher value for the $W+w$ sample, $\langle$Fe II/Mg II$\rangle_{W+w} = 8.4 \pm 1.4$, than for the N sample, $\langle$Fe II/Mg II$\rangle_N = 4.4 \pm 0.5$.

Figure 6 shows the $\Delta\alpha_{\mathrm{OX}}$ (the difference between the observed α_{OX} and that predicted from the $\alpha_{\mathrm{OX}} - L_{\mathrm{UV}}$ relation for objects within the same redshift interval of our sample)[5], an index of X-ray weakness, as a function of the Fe II/Mg II ratio. On average, the Fe II/Mg II ratio is higher in X-ray weak quasars with respect to X-ray normal ones. We also colour-coded EW C IV to compare this trend with the modest decrease in C IV with increasing X-ray weakness observed in Paper II. We assessed this trend by means of a Spearman's rank test, which yielded a correlation index of $r_S = -0.7$. A possible origin for this trend is discussed in Sect. 5, in terms of increased Fe II$_{\mathrm{UV}}$ emission in X-ray weak quasars associated with outflow-induced shocks and turbulence. The statistical uncertainty on the Fe II/Mg II ratio was estimated by fitting 100 mock spectra for each source: the flux in every spectral channel was created by adding a random value to the actual flux, extracted from a Gaussian distribution whose amplitude was set by the uncertainty value in that spectral channel. After fitting every mock sample, we computed the distribution of the Fe II/Mg II values, and set the uncertainty as the standard deviation of the distribution, after applying a 3σ clipping.

In Fig. 7 we show the estimates of Fe II/Mg II for our sample of ten quasars where the Mg II line was observed (excluding J0900+4215, which is flagged as radio bright), in comparison with other literature samples probing different redshift intervals (Dietrich et al. 2003; Maiolino et al. 2003; De Rosa et al. 2011; Mazzucchelli et al. 2017; Shin et al. 2019; Sameshima et al. 2020). We found that, on average, there is no clear trend for an evolution in the Fe II/Mg II ratio across cosmic time, which implies already chemically enriched BLR regions at high redshift. To verify this trend quantitatively, we performed a Spearman's rank order probability test by using the X-ray normal quasars only together with the other samples, in order to avoid any possible bias introduced by the boosted Fe II/Mg II ratios of X-ray weak sources. We then performed a linear fit of all the data sets together with EMCEE (Foreman-Mackey et al. 2013). The Spearman's test yielded a correlation coefficient of -0.26, revealing a mild trend of decreasing Fe II/Mg II ratio with redshift. The fit of the Fe II/Mg II$-z$ relation then provides evidence for a flat slope, confirming a non-significant evolution of this ratio across cosmic time. Although the highest redshift

---

[4] Throughout this work, the significance is reported as $m\sigma$ with $m = |\langle x_N \rangle - \langle x_{W+w} \rangle| / \sqrt{\sigma^2_{x_N}/n_N + \sigma^2_{x_{W+w}}/n_{W+w}}$, where $\langle x_i \rangle$ is the mean value, σ_i the standard deviation, and n_i the size of the i-th sample.

[5] For a more detailed discussion about how the values of $\Delta\alpha_{\mathrm{OX}}$ are evaluated, we refer to Sect. 2.3 of Paper II, and references therein.
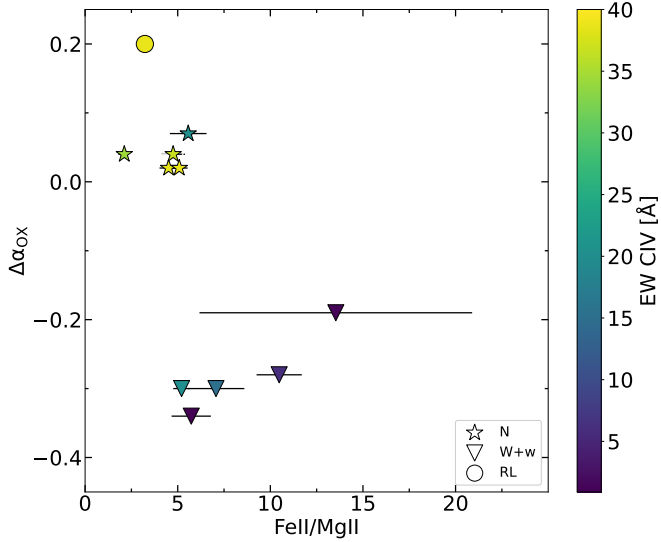
Fig. 6. $\Delta\alpha_{OX}$–(Fe II/Mg II) plane for our N (stars) and $W + w$ (triangles) sources. The radio-loud quasar J0900+4215 is shown as a circle. The $\Delta\alpha_{OX}$ value, as a proxy to X-ray weakness, is compared to the newly observed properties of the Mg II region and the relative intensity of the C IV emission (see colour bar at right). An increasing trend of the Fe II/Mg II ratio with increasing X-ray weakness can be seen.

Fig. 7. $\text{Log(Fe II/Mg II)} - z$ plane. N sources (blue stars) follow the expectations for objects at similar redshift, whereas $W+w$ sources (red triangles) are located at the top of the distribution around $z \sim 3$. The black dashed line represents the mean Fe/Mg ratio of our N quasars extrapolated over the entire redshift range.

sample from Mazzucchelli et al. (2017) exhibits systematically lower values than those at lower redshift, the same authors note that the uncertainties are so large that the consistency with a non-evolving Fe II/Mg II ratio cannot be ruled out. If we exclude this sample from the regression analysis, we find an even lower correlation coefficient (0.002), and again a slope virtually consistent with zero ($m = 0.01 \pm 0.01$). However, it is possible that, at very high redshift ($z \gtrsim 6$), we might be observing a genuine depletion of iron, symptomatic of the presence of young stellar populations in the galaxies hosting these quasars.

Our results further confirm the interpretation that samples at high redshifts, biased towards high luminosities (i.e. $L_{bol} > 10^{46} \text{ erg s}^{-1}$), presumably host SMBHs in already chemically mature galaxies (e.g. Kawakatu et al. 2003; Juarez et al. 2009). The values of their Fe II/Mg II ratios are consistent with those at lower redshifts. Possible systematic effects and a consistency check on our ability to reproduce the iron emission in our objects are discussed in Appendix C.

A strong correlation between the Fe II/Mg II ratio and the Eddington ratio has been observed, but not with the BH mass (Sameshima et al. 2017, see also Dong et al. 2011). Since the N and the $W+w$ samples are fairly homogeneous in terms of BH masses and Eddington ratios (see Sect. 5), it is unlikely that one of these parameters is the fundamental driver of the observed difference. Theoretical works using CLOUDY simulations showed that several physical properties can impact the Fe II/Mg II ratio, such as gas density and microturbulence (Verner et al. 2003; Baldwin et al. 2004; Sameshima et al. 2017; Temple et al. 2020). We will perform a detailed photoionisation modelling of the SDSS and LBT data in a dedicated publication.

4.2. Hβ properties

The nine rest frame optical spectra enabled us to investigate the properties of the Hβ–[O III] complex. We found that, on average, X-ray weak sources display a weaker Hβ emission than X-ray normal ones. The mean value of the EW for the $W+w$ group is

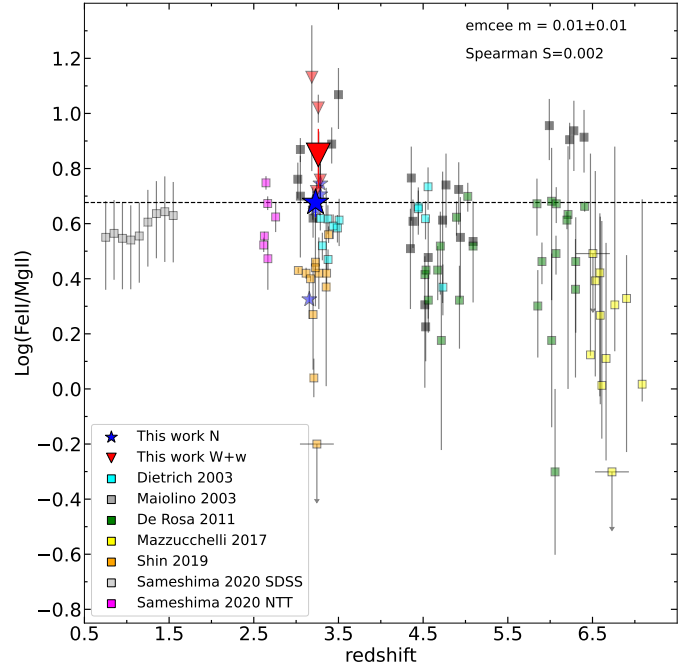$\langle\text{EW H}\beta\rangle_{W+w} = 73 \pm 8\,\text{Å}$, whereas it is $\langle\text{EW H}\beta\rangle_N = 108 \pm 11\,\text{Å}$, for the $W+w$ sample, a difference that is statistically significant at the 2.6σ level.

In order to assess whether the Fe emission of X-ray weak sources is also enhanced in the optical band, we checked the Fe II/Hβ ratio, which is a standard optical indicator of the metallicity, generally evaluated as the intensity ratio of the integrated flux of Fe II between 4434 Å and 4684 Å to that of Hβ (e.g. Boroson & Green 1992; Marziani & Sulentic 2014). The relative intensities of the optical Fe emission are statistically consistent, as we found that the average equivalent width of the optical Fe II of the N sample is $\langle\text{EW Fe II}_{opt}\rangle_N = 16 \pm 6\,\text{Å}$, whereas the $W+w$ sample yielded $\langle\text{EW Fe II}_{opt}\rangle_{W+w} = 24 \pm 9\,\text{Å}$. The ratio is $\langle\text{Fe II}_{opt}/\text{H}\beta\rangle_N = 0.14 \pm 0.06$ for the N sources, and $\langle\text{Fe II}_{opt}/\text{H}\beta\rangle_{W+w} = 0.36 \pm 0.13$ for the $W+w$ sources; therefore the mild difference between the Fe II/Hβ ratios is just mimicking the difference between the Hβ profiles of the two samples. Even so, we caution that the 4434–4684 Å interval over which the optical Fe II is generally sampled in the literature is not included in our spectra, and we thus had to rely on a full extrapolation for this estimator. For this reason, we also checked whether any difference could be found in the observed region using the equivalent width of the Fe II$_{opt}$ emission between 4900 Å and 5300 Å, which we directly observed and included in our fits. Also in this case, the difference remains marginal as the N and $W+w$ groups respectively yield $\langle\text{Fe II}_{opt}/\text{H}\beta\rangle_N = 0.31 \pm 0.07$ and $\langle\text{Fe II}_{opt}/\text{H}\beta\rangle_{W+w} = 0.72 \pm 0.32$.

The ratio of UV to optical Fe II emission is higher for X-ray weak sources, being $\langle\text{Fe II}_{UV}/\text{Fe II}_{opt}\rangle_N = 13 \pm 4$ and $\langle\text{Fe II}_{UV}/\text{Fe II}_{opt}\rangle_{W+w} = 26 \pm 9$, in line with the expectations of higher ratios of UV to optical Fe II emission for increasingly weaker SEDs in the extreme UV (EUV), as shown in Leighly et al. (2007a). We note, however, that our results are not

directly comparable with those in the third panel of Fig. 24 in Leighly et al. (2007a) since our Fe II emission data were evaluated on a much shorter interval (4900–5300 Å) than theirs (4000–6000 Å).

4.3. [O III] properties

In the context of the unified model, the [O III] is produced in the NLR, on galactic scales, and is believed to be an isotropic indicator of the AGN strength in both type I and type II AGN (e.g. Mulchaey et al. 1994; Bassani et al. 1999; Netzer 2009, and references therein). The [O III] luminosity ($L_{\mathrm{[O\,III]}}$) is a secondary indicator of the nuclear luminosity, depending on the fraction of continuum radiation within the opening angle of the torus reaching the gas in the NLR, but is also influenced by local properties such as the NLR clumpiness, its covering factor, and the amount of dust extinction (e.g. Ueda et al. 2015).

The EW [O III] value can be considered as a proxy of the inclination of our line of sight to the AGN accretion disc (e.g. Risaliti et al. 2011; Shen & Ho 2014). Bisogni et al. (2017) investigated in detail the distribution of EW [O III] in the SDSS DR7, showing that EW [O III] > 30 Å generally corresponds to high inclination angles, while lower values reflect the intrinsic EW [O III] distribution. Only one of our objects (J0303−0008) displays an EW [O III] in excess of 30 Å, thus possibly being observed at relatively high inclination (yet still likely within $\theta \lesssim 60°$, see Sect. 5). The mean (median) value of EW [O III] in our sample is 14.4 ± 7.6 (3.7) Å, or 6.6 ± 2.3 Å after excluding the strong [O III] emitter, consistent with the median value of the EW [O III] distribution from the current SDSS release (Wu & Shen 2022), which is 14.1 Å, and well below the 30 Å threshold where inclination effects should become relevant.

With the aim of putting our sample into a broader context, we compared the results concerning the [O III] emission with other samples of luminous high-redshift quasars in the literature. The sample analysed in Vietri et al. (2018), part of the WISSH survey, exhibits extremely weak [O III] profiles, with a median value of 1.5 Å. The 19 AGN at $z \sim 2$ from the SUPER sample described in Kakkad et al. (2020) yield, instead, a median value of 14.2 Å, although these sources span a wide interval in terms of bolometric luminosity ($10^{45.4}–10^{47.9}$ erg s^{-1}). When matching the SUPER sample in luminosity with our own quasars (i.e. considering only the objects with L_{bol} exceeding $10^{46.9}$ erg s^{-1}), the median value of EW [O III] decreases slightly to 11.6 Å[6]. Lastly, the median EW [O III] for the GNIRS–DQS quasars (Matthews et al. 2023) equals 12.7 Å; we note that for this sample ~15% of the sources have an unreliable EW measurements because of the weak [O III] profile. Although the cumulative EW [O III] distribution of these luminous high-redshift samples clusters around the same peak of the global SDSS quasar distribution (Wu & Shen 2022), objects with high equivalent width become relatively rare, as shown in the right side panel in Fig. 8. For instance, the fraction of objects with EW [O III] > 50 Å in the SDSS catalogue is ~10%, while the joint incidence in all the mentioned high-redshift samples is about 2%, although some systematic effects could marginally modify this estimate given
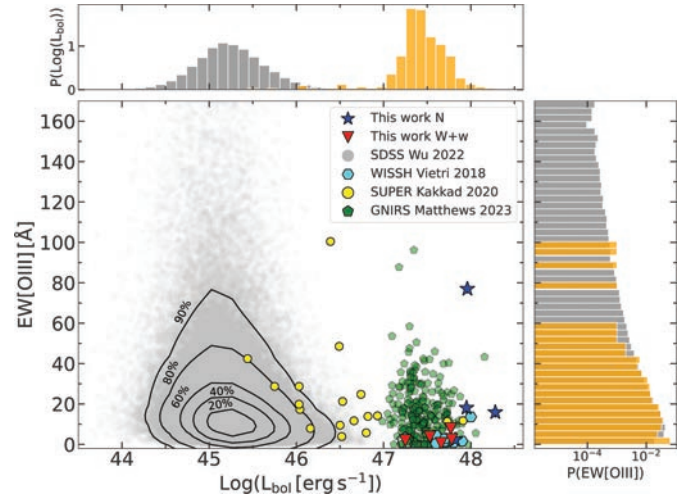

Fig. 8. Distribution of EW [O III] of our and other literature samples, as a function of bolometric luminosity. Side panels show the probability density of the quantities represented in the plot. BAL J0945+2305 is shown as an open pentagon. All but one of our objects show low EW [O III] (<30 Å), suggesting a non-edge-on line of sight. Generally, luminous high-redshift quasars tend to cluster around low EW [O III] values.

the non-uniform analysis of the different samples (e.g. continuum fitting windows, different Fe templates).

The weaker [O III] profiles in very luminous quasars with respect to the global SDSS population is likely related to the luminosity evolution of this parameter. It has been shown that the EW of the [O III] core component anti-correlates with $L_{5100\,\text{Å}}$, which can be regarded as a proxy of L_{bol} (Shen & Ho 2014). Two effects might come into play. Assuming that the intrinsic $L_{\mathrm{[O\,III]}}$ does not evolve significantly with L_{bol} (or z), the observed anti-correlation would be mainly driven by inclination, whereby high-L_{bol} high-z sources are preferentially observed with a face-on line of sight. Otherwise, if $L_{\mathrm{[O\,III]}}$ is increasing more slowly than L_{bol} (e.g. Shen 2016), we would also witness a trend of decreasing EW [O III], as for the standard Baldwin effect (Baldwin 1977; see also Sect. 4.1 of Ueda et al. 2015 for other possible effects).

As observed for other emission lines (C IV, Hβ), we generally find less prominent line profiles in $W+w$ objects also for the [O III] $\lambda\lambda$4959,5007 doublet (see also Green 1998). The mean values for the two subsamples are $\langle$EW [O III]$\rangle_N = 16.6 \pm 5.6$ Å and $\langle$EW [O III]$\rangle_{W+w} = 4.5 \pm 1.5$ Å, giving a ~2.1σ tension. In this computation we conservatively excluded from the N sample the only high-[O III] emitter, J0303−0008, whose nuclear and environmental properties have recently been investigated in Perna et al. (2023), for which inclination effects might be non negligible. The EW [O III] values of all the other sources suggest that these are likely seen at relatively low inclination instead, and hence the tentative difference between the strength of the [O III] emission in N and $W+w$ quasars could be due to intrinsic effects. At this stage, it is therefore more informative to consider $L_{\mathrm{[O\,III]}}$ rather than EW [O III]. As we do not expect any systematic difference between the geometric properties (size, covering factor) or physical properties (metallicity, density) of the NLR in X-ray weak and X-ray normal quasars, we argue that the main driver of $L_{\mathrm{[O\,III]}}$ is the line emissivity (e.g. Baskin & Laor 2005b), which ultimately depends on the shape of the EUV–soft X-ray SED.

If the range of [O III] intensities that we observe is caused by intrinsic differences in the unobservable portion of the SED,

---

[6] For the SUPER sample, EW [O III] is not directly reported by the authors, so it was estimated here as $L_{\mathrm{[O\,III]}}/L_{5100\,\text{Å}}$. This normalisation could produce a slightly overestimated EW [O III] in case of a steeply decreasing optical continuum. However, by assuming an average continuum slope $\alpha_\lambda = -0.42$ from Vanden Berk (2001), normalising at 5100 Å rather than at 5007 Å has a negligible effect on EW [O III].

a correlation with the X-ray emission should be expected, as the level of the latter determines the SED steepness. Several studies have investigated the relation between [O III] and X-ray emission, finding a high degree of correlation (e.g. Mulchaey et al. 1994; Panessa et al. 2006; Meléndez et al. 2008; Ueda et al. 2015). Because they are both proxies of the intrinsic power of the central engine, L_X and $L_{[O III]}$ are naturally expected to correlate in the case of type I objects, where the line of sight does not cross the dusty torus; the correlation holds also in type II objects, when considering absorption–corrected L_X. In Fig. 9 we show the relation between the hard (2–10 keV) X-ray and the [O III] luminosity of our quasars together with other reference samples (Panessa et al. 2006; Meléndez et al. 2008; Ueda et al. 2015). We also include the objects with currently available [O III] and X-ray data from Laurenti et al. (2022) and, in the high-luminosity tail, also those from the WISSH and SUPER samples. For the WISSH and the Laurenti et al. (2022) samples we also divided the sources into X-ray normal and X-ray weak according to their $\Delta\alpha_{OX}$ value, adopting a conservative threshold of $\Delta\alpha_{OX} \leq -0.3$ to define X-ray weakness. Objects whose [O III] emission is barely detectable are labelled as upper limits. Our sample seems to follow the trend of less luminous objects, even though, J0303−0023, because of its very faint [O III], is slightly below the other N sources. The L_X values of J0945+2305 and J1425+5406 are labelled as upper limits, being marginally detected as stated in Paper I. Remarkably, despite their weak [O III] profiles, X-ray weak objects do not drop out from the main trend of the $L_{[O III]}$− L_X relation.

We also tested, at least qualitatively, the possibility that the lower $L_{[O III]}$ in X-ray weak objects were due to dust extinction in the NLR. We did not have the possibility to use the Balmer decrement, the most straightforward way to assess local extinction, because the Hα line is not covered by our spectra. We thus assumed that N and $W+w$ quasars had intrinsically similar [O III] emission lines, but the latter subsample suffered from a greater dust extinction. Then, we considered N quasars with average [O III] emission (i.e. we excluded J0303−0023, whose emission is barely detectable, and J0304−0008, the brightest [O III] emitter) and allowed for increasing dust extinction. The detailed procedure is explained in Appendix D. Even in the case of significant reddening, $E(B - V) = 0.2$, [O III] is still clearly detectable. A high degree of extinction is also disfavoured by the locus occupied in the $\Gamma_{1450-3000\,\text{Å}} - \Gamma_{0.3-1\,\mu m}$ plane (see Fig. 2 of Paper II) by the whole sample, which was selected in order to include blue unobscured quasars.

We finally note that the [O III] profile does not generally reveal signatures of strong outflows, with the only exception of J0942+0422, where a fairly broad ($\sim$1200 km s^{-1}) component is detected, blueshifted with respect to the core component by $\sim$470 km s^{-1} (Fig. 2). It is possible, however, that in some cases, where the [O III] profile is weak and blended with Fe II$_{opt}$, any blueshifted [O III] component resulted undetectable even if present.

4.4. Relation to accretion parameters

The quasars at high redshift constituting this sample were chosen so as to display a high degree of homogeneity in the UV, being very luminous with a blue spectrum, according to the criteria described in Paper I. We then found that on the X-ray side the sources are far less homogeneous since the sample also includes a significant fraction of X-ray weak objects. We then focused on the spectroscopic optical-UV properties to find any evidence for differences accompanying the X-ray weakness in the $W+w$ sample.
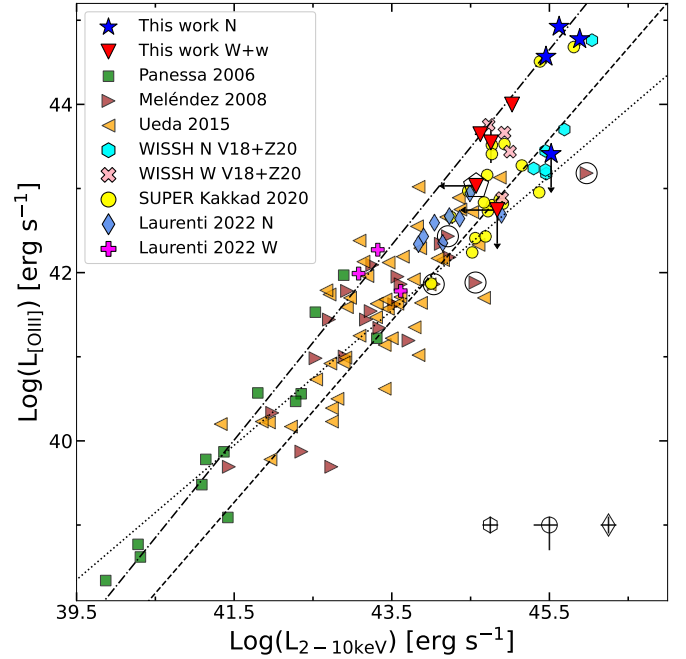

Fig. 9. Log($L_{[O III]}$)–Log($L_{2-10\,keV}$) plane. The dot-dashed, dotted, and dashed lines represent respectively the best fits for the Panessa et al. (2006), Meléndez et al. (2008), and Ueda et al. (2015) samples. Other luminous high-redshift samples with currently available [O III] and X-ray data from the WISSH (Vietri et al. 2018; Zappacosta et al. 2020) and SUPER (Kakkad et al. 2020) surveys, as well as the less luminous sample from Laurenti et al. (2022) including some X-ray weak objects, are also shown. Our objects where the [O III] is barely detectable (i.e. J0303−0023 and J1425+5406) are represented as upper limits. The circled data are defined as radio loud by the authors. BAL J0945+2305 is shown as an open pentagon. The typical uncertainties for the WISSH, SUPER, and Laurenti et al. (2022) samples are shown at the bottom of the plot.

The newly estimated (and generally more reliable for 11/29 objects) BH masses, as well as the Eddington ratios, allowed us to investigate further what the key accretion parameters of the sample are, and to test the possibility that the observed differences between the two X-ray groups could be associated with their location in this parameter space. In Fig. 10 we present the relation between the Eddington ratio and the X-ray photon index for our sample, together with other recent samples in the literature formed by both super- and sub-Eddington accretors. Although with a huge scatter, a steeper Γ is observed as λ_{Edd} increases. The Spearman's rank test for our $z \sim 3$ sample, together with other non-weak sources (shown in Fig. 10), produced a correlation index $r_S = 0.47$, lower than the values reported by Liu et al. (2021): $r_S = 0.72$ with a p-value = 1.27×10^{-8} for their full sample, and $r_S = 0.60$ with a p-value = 0.004 for the super-Eddington subsample, which represents the tightest correlation found so far for highly accreting sources.

We performed a linear regression using the module EMCEE allowing for intrinsic dispersion, removing known X-ray weak objects and sources whose Γ was fixed in the X-ray spectral analysis. The former were removed as their coronal emission is possibly experiencing a non-standard phase; the latter were removed because the poor quality of the data did not allow a simultaneous estimate of both Γ and N_H. The resulting slope is $\beta = 0.16 \pm 0.03$, somewhat flatter than other previous findings ($\beta = 0.31 \pm 0.01$, Shemmer et al. 2008; $\beta = 0.31 \pm 0.06$, Risaliti et al. 2009;
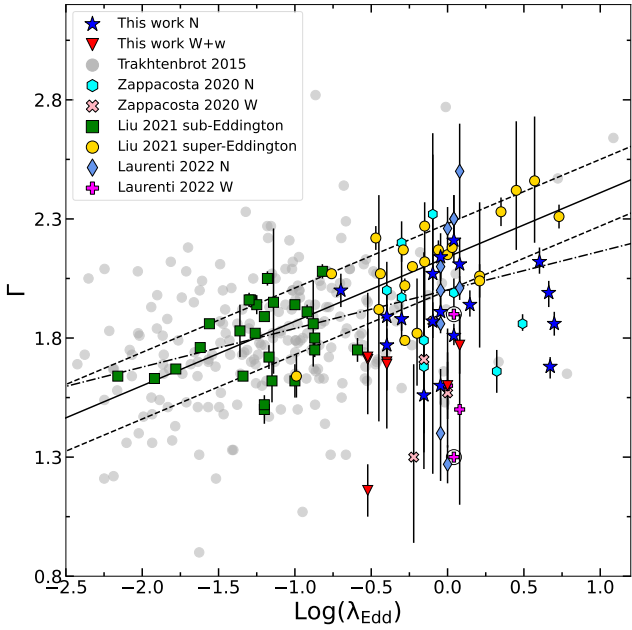
Fig. 10. Γ–Log(λ_{Edd}) plane. Highly accreting samples are labelled as indicated in the legend. Circled sources have a fixed Γ in their X-ray analysis. The black continuous line represents the best fit from Liu et al. (2021), which produced a slope $\beta = 0.27 \pm 0.04$, while the dashed line represents the 1σ dispersion. The dot-dashed line is our best fit including all the samples (except the sources from Trakhtenbrot et al. 2017, for which there was no information about possible X-ray weak sources), which results in a flatter slope $\beta = 0.16 \pm 0.03$.
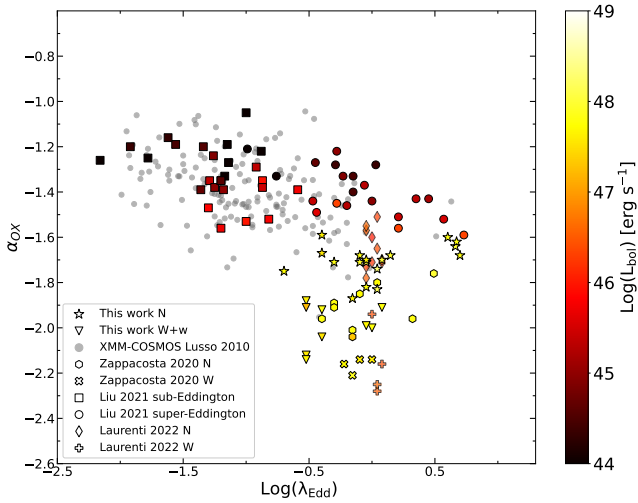

Fig. 11. α_{OX} against Log(λ_{Edd}). The different symbols refer to the different samples (see legend). The bolometric luminosity is colour-coded and, for a fixed Eddington ratio value, spans 3–4 orders of magnitude.

$\beta = 0.57 \pm 0.08$, Jin et al. 2012; $\beta = 0.32 \pm 0.05$, Brightman et al. 2013), but fully consistent with Trakhtenbrot et al. (2017), who report $\beta = 0.17 \pm 0.04$ for hard X-ray selected AGN in the *Swift*/BAT spectroscopic survey (BASS).

For 11/29 objects the UV–optical analysis yielded more robust estimates of the BH masses based on Hβ and/or Mg II. We did not find any statistically significant difference in the average M_{BH} between N and $W+w$ sources: the mean BH mass for the N group is $\langle\mathrm{Log}(M_{\mathrm{BH}}/M_\odot)\rangle_N = 9.7 \pm 0.1$, and $\langle\mathrm{Log}(M_{\mathrm{BH}}/M_\odot)\rangle_{W+w} = 9.8 \pm 0.1$ for the $W+w$ group. As this

sample was selected to have high and uniform bolometric luminosity (with a standard deviation of ∼0.1 dex), and because the BH masses are nearly identical, we also expected that the Eddington ratios should not differ significantly. The mean (median) values are $\langle\lambda_{\mathrm{Edd}}\rangle_N = 1.6 \pm 0.4$ (0.9) and $\langle\lambda_{\mathrm{Edd}}\rangle_{W+w} = 0.5 \pm 0.1$ (0.4). The slight difference between the mean (median) values is likely due to the marginally higher bolometric luminosity of the N sample, $\langle\mathrm{Log}(L_{\mathrm{bol}}/\mathrm{erg\,s^{-1}})\rangle_N = 47.84 \pm 0.04$, with respect to the $W+w$ sample, $\langle\mathrm{Log}(L_{\mathrm{bol}}/\mathrm{erg\,s^{-1}})\rangle_{W+w} = 47.58 \pm 0.06$.

The higher fraction of X-ray weak objects reported in high-λ_{Edd} quasar samples (Paper I; Zappacosta et al. 2020; Laurenti et al. 2022) compared to the general AGN population (Pu et al. 2020) hints at some modification of the interplay between the corona and the disc emission in the high-accretion regime. The strength of the emission from the corona with respect to the disc can be roughly estimated through the indicator α_{OX}. In Fig. 11 we show α_{OX} as a function of the Eddington ratio for different AGN samples. The resulting anti-correlation (Lusso et al. 2010; see also Sect. 4.2 in Liu et al. 2021, and references therein) displays a rather large spread since sources with similar λ_{Edd} can span several orders of magnitude in terms of bolometric luminosity (which ultimately governs the SED steepness).

Nonetheless, the relation should naturally tighten if we include the BH mass into the parameter space: for a given λ_{Edd}, the higher the M_{BH}, the higher the L_{bol}. Liu et al. (2021) proposed that the scatter of the relation is due to a non-edge-on view on a more fundamental plane in the $\alpha_{\mathrm{OX}} - \lambda_{\mathrm{Edd}} - M_{\mathrm{BH}}$ space. In Fig. 12 we superimpose, on the relation found by Liu et al. (2021), all the type I AGN samples shown in Fig. 11, which include the extreme BH hole mass tail of the quasar population at high redshift. Remarkably, our N quasars sit nicely on the extrapolation of the best-fit regression line, whereas the $W+w$ group drops far below, exhibiting lower α_{OX} than the other sources in the same $\lambda_{\mathrm{Edd}}-M_{\mathrm{BH}}$ domain. The α_{OX} parameter is still very steep, also for other groups of very luminous quasars such as those from Zappacosta et al. (2020) and Laurenti et al. (2022), but also the bulk of X-ray normal sources of these samples is slightly below the prediction (by ~ -0.2). Very luminous sources could behave differently from the expectations, suggesting that, if a universal relation existed, it could be steeper, or that the high and low ends of the BH mass–Eddington ratio distribution cannot be jointly described by a linear relation with α_{OX}. The sources of Liu et al. (2021), whose fit we extrapolated, were selected with criteria similar to ours, being radio-quiet, non-BAL, and with good-quality X-ray data ($S/N > 6$). However, no criteria about their optical-UV emission (e.g. luminosity, photometric indices) were applied. Moreover, in 7/48 objects with multiple X-ray data available, the authors chose the high-flux objects, and this choice can somewhat affect the comparison. Furthermore, the sources analysed in Zappacosta et al. (2020) were chosen to study the impact of outflows driven by hyperluminous quasars. It is thus possible that the mismatch between the selection criteria can also reduce the general agreement of the results. Overall, a better sampling of the very luminous, highly accreting side of the distribution will be key to assessing whether the accretion mechanism is the same on very different scales of its governing parameters.

5. Discussion

As a general consideration, two different flavours of X-ray weakness exist, as we can find both intrinsic and apparent X-ray weak sources. The former are likely associated with the physics
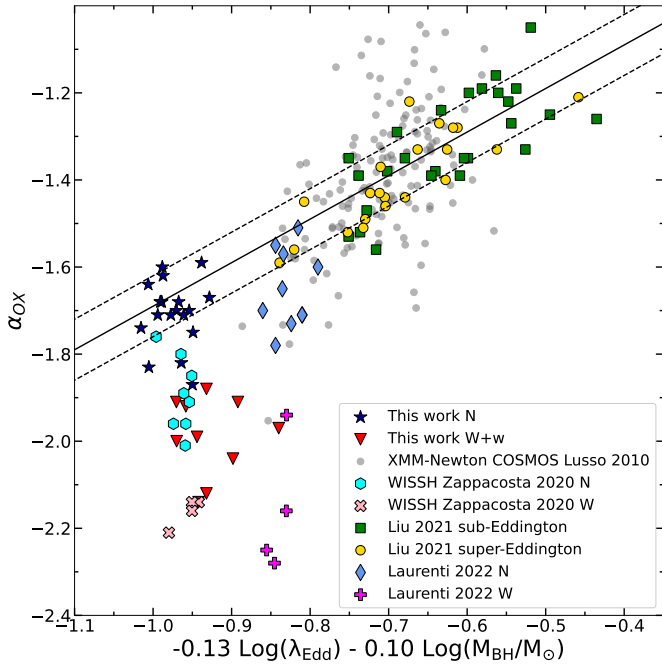
Fig. 12. Edge-on view on the $\alpha_{OX} - \lambda_{Edd} - M_{BH}$ space. The various samples are listed in the legend. The solid line is the best regression as found by Liu et al. (2021), while the dashed lines represent the 1σ dispersion. Quasars with high BH masses and high accretion rates extend the range of the relation. The bulk of our X-ray normal sources follow the extrapolation of the relation calibrated on less luminous sources at lower redshifts.

of the corona, which is not efficiently producing the normal X-ray emission, and we witness a wide range of weakness factors and photon indices. PHL 1811 is the most extreme case of the first kind, given its very steep photon index $2.0 < \Gamma < 2.6$ (but see Wang et al. 2022), the variability, and the ∼2 orders of magnitude weakness. The latter are instead related to some kind of absorption (e.g. slim disc, failed and/or clumpy wind, warm absorber) along the line of sight. Our objects do not clearly fit in either of these two classes, being in some way intermediate between them, showing flatter ($\Gamma \lesssim 1.7$) spectra in the absence of clear absorption and moderate weakness factors. This is why it is important to understand their prevalence among the AGN population and their underlying physics.

The analysis of the X-ray data in Paper I revealed an anomalously high fraction (≈25%) of X-ray weak (≳3–10 times fainter than expected) objects. Although in some cases (the few marginal detections, plus J1201+01 and J1459+0024) the quality of the data is not good enough to completely rule out some level of absorption, in general a column density exceeding $N_H(z) > 3 \times 10^{22}$ cm^{-2} can be ruled out. This is a consequence of the lack of any cutoff around 1 keV associated with X-ray absorption.

In Paper II we found a correlation between X-ray and C IV luminosity, which holds for X-ray normal objects over the whole range probed by an extended control sample ($10^{43.5}–10^{45.5}$ erg s^{-1} in $L_{2\,keV}$ and $10^{43}–10^{46}$ erg s^{-1} in $L_{C\,IV}$), whereas X-ray weak sources lie below that main sequence. In absolute terms, X-ray weak objects present more luminous C IV lines than expected for quasars with similar X-ray luminosity. Even so, X-ray weakness might lead to a less efficient population of the excited level (∼8 eV above the ground state) that is collisionally excited because of the X-ray heating

of the gas. We argue that such a relation (holding for the N sources) is probably a by-product of the more general $\alpha_{OX} - L_{UV}$ relation.

With respect to N quasars, $W + w$ quasars do not show strikingly different blueshifts of the C IV line with respect to N quasars, but on average shallower (i.e. broader and less prominent) line profiles. This could be due to two reasons (at least): (i) fast, mostly equatorial outflows are present among X-ray weak quasars, but our low-inclined line of sight offsets their observational footprints, and (ii) the difference in C IV emission between N and $W+w$ objects is caused by some mechanism affecting the region where the photons producing the C IV come from. By analysing ∼190 000 spectra from the seventeenth SDSS data release, Temple et al. (2023) find that high (≥1000 km s^{-1}) median C IV blueshifts are observed only in quasars with high SMBH masses ($M_{BH} \geq 10^9 M_\odot$) and high Eddington ratios ($\lambda_{Edd} \geq 0.2$). The $z \sim 3$ sample analysed here fulfils both requirements of high BH masses and high Eddington ratios, so all the sources could be, in principle, in the outflow phase. The fact that we observe C IV blueshifts around or slightly less than 1000 km s^{-1}, on average, can be explained as a projection effect whereby mostly equatorial winds are observed under low inclination angles. In this framework the fraction of X-ray weak objects could be related to the wind duty cycle (e.g. Fiore et al. 2023), which is otherwise poorly known. We can set a lower limit to the wind persistence based on the concomitant [O III] weakness. Assuming the relation for the single-zone [O III]-emitting region described in Baskin & Laor (2005b), which is $R_{NLR} = 40 (\lambda L_\lambda/10^{44})^{0.45}$ pc, where $\lambda L_\lambda \sim 10^{47}$ erg s^{-1} for our objects, we obtain $R_{NLR} \approx 1$ kpc. Hence, it would take $t \sim R_{NLR}/c \sim 3000$ yr for the NLR to respond to changes in the nuclear activity. Considering that the longer light-travel time within the NLR would dilute any more rapid nuclear flickering, the wind lifetime should be at least ≈10^4 yr.

In addition, we find a qualitative similarity between the X-ray normal and weak UV stacks in the top panel of Fig. 7 in Paper II, and the C IV core and wind-dominated stacks depicted in Fig. 5 of Temple et al. (2021), where the N ($W+w$) stack is more similar to the C IV core-dominated (wind-dominated) one. The $W+w$ and wind-dominated stacks share the broader and shallower line profile and the flatter continuum, although the latter spectrum exhibits more extreme properties in terms of lower line equivalent width and higher offset velocity than ours.

In principle, the lack of seed photons causing the lower intensity of the C IV emission could be due to some kind of shielding triggered by the high-accretion regime: a puffed-up disc (e.g. Luo et al. 2015) could prevent ionising photons from reaching the BLR and intercept part of the X-ray emission, causing absorption along the line of sight. According to this model, our line of sight should cross the absorber, thus favouring a more edge-on geometry (still preserving the type I nature of these AGN). Considering the thickness of the disc bulge and its density, we should thus detect absorption in the X-rays well in excess of $N_H \gtrsim 10^{23}$ cm^{-2}, but our sample does not fulfil this condition.

In Sect. 4.2 we reported higher values of EW Hβ for the X-ray normal sources with respect to the weak ones. We checked other samples containing X-ray weak sources with available optical data, finding a similar behaviour. The average values for N and W objects in the WISSH sample described in Vietri et al. (2018) are $\langle$EW H$\beta\rangle_N = 62 \pm 7$ Å and $\langle$EW H$\beta\rangle_W = 47 \pm 7$ Å, different at the ∼1.6σ level. A statistically more significant difference is found for the objects analysed in Laurenti et al. (2022),

for which the SDSS data from the Wu & Shen (2022) catalogue yield the values $\langle \text{EW H}\beta \rangle_N = 51 \pm 6\,\text{Å}$ and $\langle \text{EW H}\beta \rangle_W = 25 \pm 4\,\text{Å}$, giving a $\sim 3.7\sigma$ tension[7].

We thoroughly discussed the [O III] properties and the relation between the [O III] and X-ray emission in our sample in Sect. 4.3. The low ($<30\,\text{Å}$) EW suggests that inclination does not play a major role in our findings, as it is generally regarded to be significant for EW [O III] $> 30\,\text{Å}$. Highly inclined ($\theta > 60°$) lines of sight are also disfavoured by a luminosity argument. Assuming, for instance, a 75° inclination, which might still not intercept the dusty torus at these luminosities (e.g. Sazonov et al. 2015), the geometric correction $1/\cos\theta$ would yield a factor of $\simeq 4$, shifting the average $\text{Log}(L_{\text{bol}}/\text{erg s}^{-1})$ of our $z \sim 3$ quasars upwards by 0.6 dex to ~ 48.4, when only one source in the entire Wu & Shen (2022) catalogue has a higher luminosity.

Weaker [O III] profiles, as discussed in Sect. 4.3, are generally found with increasing L_{bol}, which is likely due to an intrinsic decrease in the $L_{\text{[O III]}}$ with respect to the continuum and, to a lesser extent, to an inclination effect whereby more luminous objects are preferentially observed at smaller polar angles. Finally, the possibility of a reduced [O III] emission because of extinction in the NLR of X-ray weak sources is disfavoured (see Appendix D), and would call for an unknown causal connection between very different scales (i.e. $\sim 10^{-3}$ and 10^3 pc).

We also observed a trend of higher EW Fe II$_{\text{UV}}$ and Fe II/Mg II ratio for X-ray weak sources, in line with the expectations for prototypical X-ray weak quasars (see e.g. the analyses of PHL 1811 by Leighly et al. 2007a,b). These, and some other features characterizing X-ray weak objects, are consistent with the trends expected in the 4D Eigenvector 1 (4DE1; Sulentic et al. 2000). The transition between the so-called populations B and A (mainly driven by accretion rate and orientation, see e.g. Shen & Ho 2014) happens with the increase of the optical Fe emission, the offset velocity of the C IV emission line, and a decrease of the equivalent of the width of the C IV and EW [O III] emission lines (see respectively supplementary Figs. E4 and 1 in main text in Shen & Ho 2014). We note that the exact position of our objects along the 4DE1 main sequence is unclear. We cannot evaluate the canonical estimator R_{Fe} ($R_{\text{Fe}} = \text{EW Fe II}_{\text{opt}}/\text{EW H}\beta$) as the 4434–4684 Å optical Fe complex falls just bluewards of our K_S spectra. Even assuming the 4900–5300 Å interval as a proxy of the canonical one, the two samples are not segregated in the FWHM Hβ–R_{Fe} plane. Considering their uncertain position along the R_{Fe} axis and the homogeneity of our sources in terms of accretion rate and orientation, which are believed to be the main drivers along the sequence, it is not straightforward to understand the differences between the N and $W+w$ sources within the 4DE1 formalism.

This notwithstanding, we need to piece together all the available observational evidence in order to find a mechanism capable of explaining the following results on the $W+w$ sources: (i) X-ray weakness in the absence of clear X-ray absorption (which still cannot be ruled out in some objects); (ii) the generally weaker and shallower line profile of C IV (and optical lines such as Hβ and [O III]), although still more luminous than expected for nor-

mal quasars with similar X-ray luminosity; (iii) the tentative trend of higher Fe II/Mg II.

The generally larger incidence of X-ray weak objects in highly accreting samples also deserves some further considerations. Several studies have recently pointed out that the fraction of X-ray weak quasars could be enhanced when the objects are accreting at near-Eddington rates. Zappacosta et al. (2020) found that about 40% of their sources (belonging to the WISSH sample) have $\Delta\alpha_{\text{OX}} < -0.3$ and also display C IV shifts of over $5000\,\text{km s}^{-1}$, but the column density of the absorber is generally (in three out of four objects) below $10^{23}\,\text{cm}^{-2}$. The same trend at lower luminosity ($L_{\text{bol}} = 10^{46.0}-10^{46.6}\,\text{erg s}^{-1}$) and redshift ($z \simeq 0.4-0.7$) is observed in the sample analysed by Laurenti et al. (2022), where $\sim 30\%$ of their objects exhibit X-ray weakness without requiring absorption. Conversely, the high-λ_{Edd} sample of Liu et al. (2021) does not contain any X-ray weak object as the lowest value of $\Delta\alpha_{\text{OX}}$ is -0.14. This sample is made of less luminous ($L_{\text{bol}} < 10^{46.3}\,\text{erg s}^{-1}$) low-redshift ($z \leq 0.25$) quasars. It is worth noting that the authors selected the sample discarding, among the other criteria, X-ray and UV–optical absorbed sources, and choosing the X-ray high-flux state in case of multiple observations. The latter selection criterion could partially explain the lack of X-ray weak objects.

It is also possible that variability is enhanced in highly accreting objects (e.g. Ni et al. 2020), and some of the observed weakness could be due to negative fluctuations. However, all the objects with multiple observations (see Sect. 5.1 and Table 3 in Paper I) do not show transitions between the W and N states. Another example of a persistent X-ray weak condition is shown in Laurenti et al. (2022): J0300−08 was targeted in 2011 by the *Neil Gehrels Swift* Observatory (Gehrels et al. 2004), then observed by *XMM-Newton* in 2018 and again by *Swift* in 2021. All these observations (*Swift* only provided 3σ upper limits) reported an X-ray flux below the expectations. Generally speaking, it is possible that a high accretion rate can enhance the possibility of finding a quasar in an X-ray weak state, and can provide clues about the possible underlying mechanism (e.g. a shielding wind, a photon-trapping disc, a puffed-up slim disc).

Putting together all the pieces of information we have, our best phenomenological guess is represented by the sketch in Fig. 13. Specifically, a powerful outflowing phase depletes the inner region of the accretion disc, causing a dearth of the seed UV radiation feeding the coronal X-ray emission, while part of the UV radiation is powering the wind. The change in the local accretion rate can have little impact on the near- to far-UV SED, but a more dramatic effect on the extreme UV (inaccessible to observations) and X-ray emission. If the corona is starved and intrinsically weak, X-ray weakness can be explained without invoking any shielding, which, otherwise, would require moderate to high inclination. The low-inclination perspective is in line with the observed high luminosity, the mild blueshift of the C IV line (due to the mostly equatorial propagation of radiatively driven winds; e.g. Proga 2003), and the small values of EW [O III] (which, however, also depend on the SED shape).

Despite the reduced X-ray heating, the C IV emission is weaker but not suppressed since an ample reservoir of ionising photons is still present at high luminosities. Moreover, a crucial contribution to the strength of the C IV line also comes from the X-ray heating of the gas, which, by means of electron–ion collisions, populates the C IV excited state. Krolik & Kallman (1988) determined the energy of the continuum photons mainly contributing to the line emission for the most important emission lines, based on different continuum assumptions between $\sim 0.01-2\,\text{keV}$. Both C IV and Hβ rely on the Lyman continuum

---

[7] In both of these samples the average EW Hβ is smaller than for our sources, for which the line falls close to the edge of the K_S spectra and the absolute value of its equivalent width strongly depends on the exact placement of the continuum and on the adopted iron template. However, the relative difference between N and $W+w$ objects goes in the same direction in all three samples.
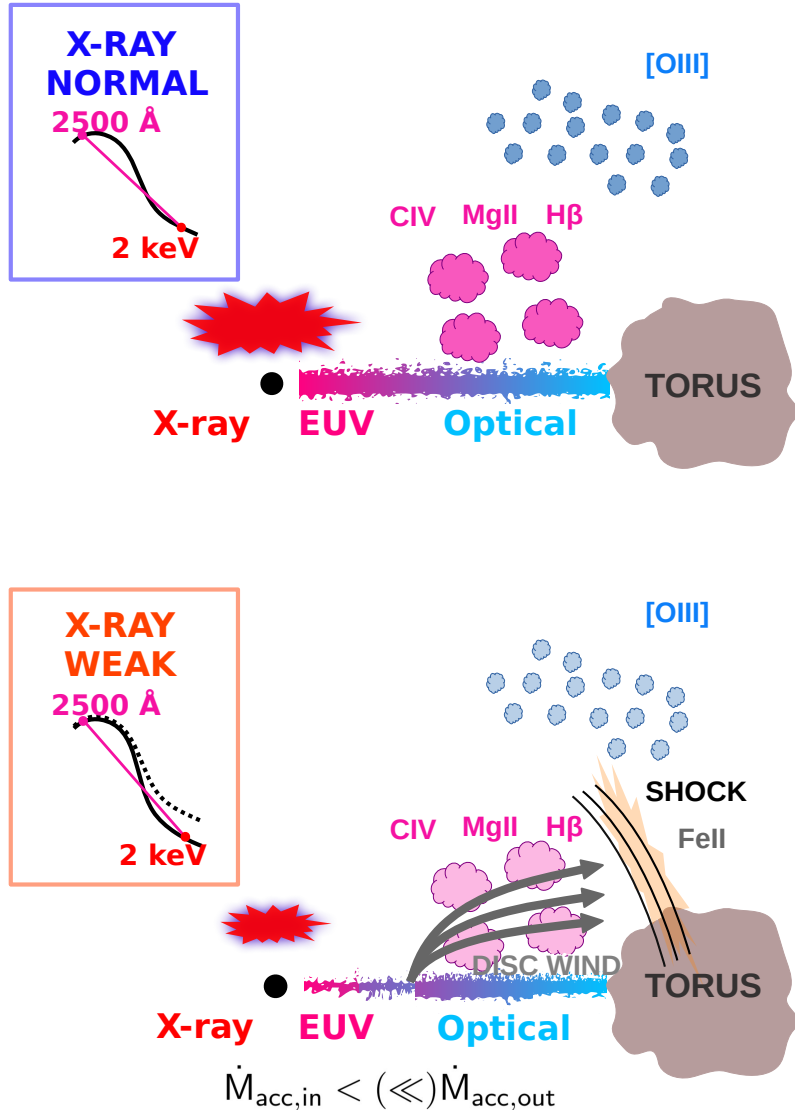
Fig. 13. Sketch of the observational features of X-ray normal (top) and weak (bottom) quasars. In the weak case a powerful wind affects the X-ray coronal emission. The outflowing phase depletes the UV-radiating inner disc, and the Comptonisation process falls short of seed radiation. The resulting X-ray flux is thus reduced without the need for absorption. Shocks at the interface between the disc wind and the BLR gas can enhance the Fe II/Mg II ratio in X-ray weak sources. The observer is assumed to be on top, but a rather wide range of viewing angles remains compatible with the type I nature of these sources. Since our line of sight is not expected to be significantly inclined with respect to the disc axis, as suggested by the very high bolometric luminosity of the sample and confirmed by the low EW [O III], outflow footprints like absorption dips or strong blue wings in C IV could be hidden. On larger scales, the [O III] luminosity mimics the X-ray behaviour, being lower in the X-ray weak sample, but fully consistent with the high-luminosity extrapolation of the $L_{[O III]}-L_X$ relation. The weaker line emission in X-ray weak sources, here depicted by more tenuous colours, is associated with the difference in the SED shape, as systematic differences between the BLR/NLR in X-ray weak and normal sources are not expected. This a mechanism is more likely to be found in highly accreting sources, where conditions are conducive to the launch of powerful winds, and hence the enhanced X-ray weak fraction in high λ_{Edd} objects.

photons between 13.6–24.5 eV, and also on the continuum intensity at 300–400 eV and 300–800 eV, respectively, which is likely suppressed in the SED of X-ray weak objects, producing the generally lower equivalent widths observed in such sources.

On the other hand, the higher incidence of Fe II/Mg II is rather puzzling. A high value of Fe II/Mg II ~ 15.5 (Leighly et al. 2007a,b) is observed in the prototypical intrinsically X-ray weak quasar PHL 1811, but in that case it is accompanied by a soft ($\Gamma = 2.3 \pm 0.1$) X-ray emission, which we do not report here for our $W+w$ sources. Weakness in our sample is accompanied by flatter photon indices than the average $\Gamma = 1.9$ (Piconcelli et al. 2005; Bianchi et al. 2009a) found in the unobscured quasar population. Following Leighly et al. (2007b, see

their Fig. 24 and the relative SED in Fig. 11 in Casebeer et al. 2006), increasingly EUV-deficient SEDs would produce higher values of both Fe II/Mg II and Fe II$_{UV}$/Fe II$_{opt}$. For our sample we observe an average Fe II/Mg II value of 4.4 for N and 8.4 for $W+w$, which is consistent with a softer EUV SED for X-ray weak with respect to X-ray normal objects. In addition the average values for Fe II$_{UV}$/Fe II$_{opt}$ are qualitatively in line with the predictions in Leighly et al. (2007b), with 13 ± 4 for the N and 26 ± 9 for the $W+w$ subsample (see Sect. 4.2).

There have been claims (e.g. Sameshima et al. 2011, Temple et al. 2020) that the Fe II emission could be enhanced by the presence of shocks and microturbulence, as already noted in Baldwin et al. (2004), which, in our scenario, could be possi-

bly linked to the outflowing phase. Shocks from the disc wind could thus facilitate the formation of the Fe II pseudo continuum in parallel to the main ionisation process due to the coronal emission. This could link, at least phenomenologically, X-ray weakness to the higher Fe II$_{\rm UV}$/Mg II that we observe. Further analyses are needed to thoroughly investigate this suggestion: collecting simultaneous and gapless spectra from the rest frame optical to the UV (a task currently possible for the $z \sim 3$ sample with a ground-based spectrograph such as VLT X-SHOOTER) would definitely improve the reliability of the analysis and our understanding of the impact on the line properties of the different regions of the SED in X-ray weak and normal objects.

6. Conclusions

In this third paper in the series, we presented the optical and middle UV analysis of the $z \sim 3$ quasars whose X-ray and far-UV spectral properties were described, respectively, in Nardini et al. (2019b) and in Lusso et al. (2021). The main goal pursued in this work was to investigate additional spectral features that can distinguish X-ray weak ($W+w$) from X-ray normal (N) quasars. To this end, we were awarded dedicated observations at the Large Binocular Telescope in both the rest frame UV and optical bands, respectively observed in the zJ and K_S bands between 2018 and 2021.

Our main findings are listed below:

– We confirm, by combining C IV, Mg II, and Hβ virial mass estimates, that the black holes hosted in these high-redshift quasars belong to the very high-mass tail of the BH mass distribution. Their masses had already grown up to $\sim 10^9 - 10^{10}\,M_\odot$ when the Universe was about 2 Gyr old. Given the bolometric luminosity estimated from the 1350 Å monochromatic flux, we derived the Eddington ratio for each object, confirming that the whole sample is made of highly accreting quasars ($\lambda_{\rm Edd} \sim 0.1$–5, with a median of 0.9).
– By fixing the slope of the continuum in order to match that of the SDSS counterpart, we find that $W+w$ objects generally exhibit more prominent Fe II$_{\rm UV}$ emission and, in turn, higher Fe II/Mg II ratios with respect to N objects. Wind-related microturbulence and shocks in outflows could enhance the Fe II production in X-ray weak sources.
– Comparing our estimates of the Fe II/Mg II ratios of the N objects with other literature samples, we found that they are in line with the expectations for quasars at similar redshifts. We also confirm that there is no evidence for an evolving ratio across cosmic time up to $z \sim 6.5$, pointing towards a prior chemical enrichment of the BLRs.
– The EW [O III] emission is generally low (<20 Å) in all but one of our objects. This suggests that inclination effects do not play a major role, as sources observed under high viewing angles usually display EW [O III] $\gtrsim 30$ Å. The lower EW of several emission lines (C IV, Hβ, [O III]) in X-ray weak quasars could be related to the decrease of EUV photons responsible for the line production. The $L_{\rm [O III]}$ of the X-ray weak and normal quasars are consistent with the high-luminosity extrapolation of the $L_{\rm [O III]}-L_{2-10\,\rm keV}$ relation from other samples in literature.
– The presence of a mostly equatorial disc wind could explain all the observational features that we have reported so far. Part of the UV radiation would not be reprocessed in the X-ray corona causing intrinsic X-ray weakness (i.e. not due to absorption). In the case of modest inclination of the line of sight to the disc, consistent with the EW [O III] values

that we find and with the huge bolometric luminosities, we could be missing the typical footprints of an outflow such as a prominent blue wing or absorption dips in the C IV profile. A higher Fe II$_{\rm UV}$ emission in X-ray weak quasars could be attributed to microturbulence and shocked regions at the interface between the outflow and the BLR medium.

In this third paper in the series we further demonstrated that X-ray weak and X-ray normal quasars also show different trends in their emission-line properties. Nearly simultaneous observations at rest frame optical–UV wavelengths and in X-rays are key to constraining the broadband ionising continuum in both populations. In the future, the results of our analysis need to be confirmed on statistically larger quasar samples, possibly extending at both lower and higher redshifts to better study the evolution of the X-ray weakness fraction and of the related emission-line properties.

References

Abazajian, K. N., Adelman-McCarthy, J. K., Agüeros, M. A., et al. 2009, ApJS, 182, 543
Abramowicz, M. A., Czerny, B., Lasota, J. P., & Szuszkiewicz, E. 1988, ApJ, 332, 646
Adelman-McCarthy, J. 2008, ApJS, 175, 297
Ageorges, N., Seifert, W., Jütte, M., et al. 2010, SPIE Conf. Ser., 7735, 77351L
Agostino, C. J., Salim, S., Ellison, S. L., Bickley, R. W., & Faber, S. M. 2023, ApJ, 943, 174
Ahumada, R., Prieto, C. A., Almeida, A., et al. 2020, ApJS, 249, 3
Avni, Y., & Tananbaum, H. 1986, ApJ, 305, 83
Baldwin, J. A. 1977, ApJ, 214, 679
Baldwin, J., Ferland, G. J., Korista, K., Hamann, F., & LaCluyzé, A. 2004, ApJ, 615, 610
Bañados, E., Venemans, B. P., Mazzucchelli, C., et al. 2018, Nature, 553, 473
Barth, A. J., Martini, P., Nelson, C. H., & Ho, L. C. 2003, ApJ, 594, L95
Baskin, A., & Laor, A. 2005a, MNRAS, 356, 1029
Baskin, A., & Laor, A. 2005b, MNRAS, 358, 1043
Bassani, L., Dadina, M., Maiolino, R., et al. 1999, ApJS, 121, 473
Bianchi, S., Fonseca Bonilla, N., Guainazzi, M., Matt, G., & Ponti, G. 2009a, A&A, 501, 915
Bianchi, S., Guainazzi, M., Matt, G., Fonseca Bonilla, N., & Ponti, G. 2009b, A&A, 495, 421
Bisogni, S., Marconi, A., & Risaliti, G. 2017, MNRAS, 464, 385
Bongiorno, A., Maiolino, R., Brusa, M., et al. 2014, MNRAS, 443, 2077
Boroson, T. A., & Green, R. F. 1992, ApJS, 80, 109
Brightman, M., Silverman, J., Mainieri, V., et al. 2013, MNRAS, 433, 2485
Casebeer, D. A., Leighly, K. M., & Baron, E. 2006, ApJ, 637, 157
Chen, L.-H., & Wang, J.-M. 2004, ApJ, 614, 101
Coatman, L., Hewett, P. C., Banerji, M., et al. 2017, MNRAS, 465, 2120
Cristiani, S., Trentini, S., La Franca, F., et al. 1996, A&A, 306, 395
Czerny, B., & Elvis, M. 1987, ApJ, 321, 305
Dalla Bontà, E., Peterson, B. M., Bentz, M. C., et al. 2020, ApJ, 903, 112
Davies, R. I. 2007, MNRAS, 375, 1099
Denney, K. D. 2012, ApJ, 759, 44
De Rosa, G., Decarli, R., Walter, F., et al. 2011, ApJ, 739, 56
De Rosa, G., Venemans, B. P., Decarli, R., et al. 2014, ApJ, 790, 145

Dietrich, M., Hamann, F., Appenzeller, I., & Vestergaard, M. 2003, ApJ, 596, 817

Dong, X.-B., Wang, J.-G., Ho, L. C., et al. 2011, ApJ, 736, 86

Ferland, G. J., Porter, R., Van Hoof, P., et al. 2013, Rev. Mex. Astron. Astrofís., 49, 137

Ferrarese, L., & Merritt, D. 2000, ApJ, 539, L9

Fiore, F., Gaspari, M., Luminari, A., Tozzi, P., & De Arcangelis, L. 2023, A&A, submitted [arXiv:2304.12696]

Fitzpatrick, E. L. 1999, PASP, 111, 63

Foreman-Mackey, D., Hogg, D. W., Lang, D., & Goodman, J. 2013, PASP, 125, 306

Freudling, W., Corbin, M. R., & Korista, K. T. 2003, ApJ, 587, L67

Gargiulo, A., Fumana, M., Bisogni, S., et al. 2022, MNRAS, 514, 2902

Gebhardt, K., Bender, R., Bower, G., et al. 2000, ApJ, 539, L13

Gehrels, N., Chincarini, G., Giommi, P., et al. 2004, ApJ, 611, 1005

Gordon, K. D., Fouesneau, M., Arab, H., et al. 2016, ApJ, 826, 104

Green, P. J. 1998, ApJ, 498, 170

Green, P. J., Aldcroft, T. L., Richards, G. T., et al. 2009, ApJ, 690, 644

Haardt, F., & Maraschi, L. 1993, ApJ, 413, 507

Hunter, J. D. 2007, Comput. Sci. Eng., 9, 90

Iwamuro, F., Motohara, K., Maihara, T., et al. 2002, ApJ, 565, 63

Iwamuro, F., Kimura, M., Eto, S., et al. 2004, ApJ, 614, 69

Jiang, L., Fan, X., Vestergaard, M., et al. 2007, AJ, 134, 1150

Jiang, Y.-F., Stone, J. M., & Davis, S. W. 2014, ApJ, 784, 169

Jiang, Y.-F., Davis, S. W., & Stone, J. M. 2016, ApJ, 827, 10

Jiang, Y.-F., Blaes, O., Stone, J. M., & Davis, S. W. 2019, ApJ, 885, 144

Jin, C., Ward, M., & Done, C. 2012, MNRAS, 425, 907

Juarez, Y., Maiolino, R., Mujica, R., et al. 2009, A&A, 494, L25

Just, D. W., Brandt, W. N., Shemmer, O., et al. 2007, ApJ, 665, 1004

Kakkad, D., Mainieri, V., Vietri, G., et al. 2020, A&A, 642, A147

Kawakatu, N., Umemura, M., & Mori, M. 2003, ApJ, 583, 85

Kawara, K., Murayama, T., Taniguchi, Y., & Arimoto, N. 1996, ApJ, 470, L85

King, A. 2005, ApJ, 635, L121

King, A., & Pounds, K. 2015, ARA&A, 53, 115

Kratzer, R. M., & Richards, G. T. 2015, AJ, 149, 61

Krolik, J. H., & Kallman, T. R. 1988, ApJ, 324, 714

Kroupa, P., Subr, L., Jerabkova, T., & Wang, L. 2020, MNRAS, 498, 5652

Kurk, J. D., Walter, F., Fan, X., et al. 2007, ApJ, 669, 32

Laurenti, M., Piconcelli, E., Zappacosta, L., et al. 2022, A&A, 657, A57

Leighly, K. M., Halpern, J. P., Jenkins, E. B., & Casebeer, D. 2007a, ApJS, 173, 1

Leighly, K. M., Halpern, J. P., Jenkins, E. B., et al. 2007b, ApJ, 663, 103

Liu, H., Luo, B., Brandt, W., et al. 2021, ApJ, 910, 103

Luo, B., Brandt, W. N., Hall, P. B., et al. 2015, ApJ, 805, 122

Lusso, E., & Risaliti, G. 2016, ApJ, 819, 154

Lusso, E., Comastri, A., Vignali, C., et al. 2010, A&A, 512, A34

Lusso, E., Worseck, G., Hennawi, J. F., et al. 2015, MNRAS, 449, 4204

Lusso, E., Risaliti, G., Nardini, E., et al. 2020, A&A, 642, A150

Lusso, E., Nardini, E., Bisogni, S., et al. 2021, A&A, 653, A158

Lynden-Bell, D. 1969, Nature, 223, 690

Maiolino, R., Juarez, Y., Mujica, R., Nagar, N., & Oliva, E. 2003, ApJ, 596, L155

Marconi, A., & Hunt, L. K. 2003, ApJ, 589, L21

Markwardt, C. B. 2009, ASP Conf. Ser., 411, 251

Marziani, P., & Sulentic, J. W. 2014, Adv. Space Res., 54, 1331

Marziani, P., Sulentic, J., Zwitter, T., Dultzin-Hacyan, D., & Calvani, M. 2001, ApJ, 558, 553

Matthews, B. M., Dix, C., Shemmer, O., et al. 2023, ApJ, 950, 95

Mazzucchelli, C., Bañados, E., Venemans, B., et al. 2017, ApJ, 849, 91

Mejía-Restrepo, J. E., Trakhtenbrot, B., Lira, P., Netzer, H., & Capellupo, D. M. 2016, MNRAS, 460, 187

Meléndez, M., Kraemer, S., Armentrout, B., et al. 2008, A&A, 682, 94

Moré, J. J. 1978, Numerical Analysis (Springer), 105

Mortlock, D. J., Warren, S. J., Venemans, B. P., et al. 2011, Nature, 474, 616

Mulchaey, J. S., Koratkar, A., Ward, M. J., et al. 1994, ApJ, 436, 586

Nardini, E., Reeves, J., Gofford, J., et al. 2015, Science, 347, 860

Nardini, E., Lusso, E., & Bisogni, S. 2019a, MNRAS, 482, L134

Nardini, E., Lusso, E., Risaliti, G., et al. 2019b, A&A, 632, A109

Netzer, H. 2009, MNRAS, 399, 1907

Ni, Q., Brandt, W. N., Yi, W., et al. 2020, ApJ, 889, L37

Ohsuga, K., & Mineshige, S. 2011, ApJ, 736, 2

Panessa, F., Bassani, L., Cappi, M., et al. 2006, A&A, 455, 173

Perna, M., Arribas, S., Marshall, M., et al. 2023, A&A, submitted [arXiv:2304.06756]

Piconcelli, E., Jimenez-Bailón, E., Guainazzi, M., et al. 2005, A&A, 432, 15

Proga, D. 2003, ApJ, 585, 406

Proga, D. 2005, ApJ, 630, L9

Pu, X., Luo, B., Brandt, W., et al. 2020, ApJ, 900, 141

Rakshit, S., Stalin, C., & Kotilainen, J. 2020, ApJS, 249, 17

Richards, G. T., Vanden Berk, D. E., Reichard, T. A., et al. 2002, AJ, 124, 1

Richards, G. T., Lacy, M., Storrie-Lombardi, L. J., et al. 2006, ApJS, 166, 470

Risaliti, G., & Lusso, E. 2015, ApJ, 815, 33

Risaliti, G., & Lusso, E. 2019, Nat. Astron., 3, 272

Risaliti, G., Young, M., & Elvis, M. 2009, ApJ, 700, L6

Risaliti, G., Salvati, M., & Marconi, A. 2011, MNRAS, 411, 2223

Robitaille, T. P., Tollerud, E. J., Greenfield, P., et al. 2013, A&A, 558, A33

Sądowski, A., Narayan, R., McKinney, J. C., & Tchekhovskoy, A. 2014, MNRAS, 439, 503

Salpeter, E. E. 1964, ApJ, 140, 796

Sameshima, H., Maza, J., Matsuoka, Y., et al. 2009, MNRAS, 395, 1087

Sameshima, H., Kawara, K., Matsuoka, Y., et al. 2011, MNRAS, 410, 1018

Sameshima, H., Yoshii, Y., & Kawara, K. 2017, ApJ, 834, 203

Sameshima, H., Yoshii, Y., Matsunaga, N., et al. 2020, ApJ, 904, 162

Sazonov, S., Churazov, E., & Krivonos, R. 2015, MNRAS, 454, 1202

Schlegel, D. J., Finkbeiner, D. P., & Davis, M. 1998, ApJ, 500, 525

Scodeggio, M., Franzetti, P., Garilli, B., et al. 2005, PASP, 117, 1284

Shakura, N. I., & Sunyaev, R. A. 1973, A&A, 24, 337

Shemmer, O., Brandt, W., Netzer, H., Maiolino, R., & Kaspi, S. 2008, ApJ, 682, 81

Shen, Y. 2013, Bull. Astron. Soc. India, 41, 61

Shen, Y. 2016, ApJ, 817, 55

Shen, Y., & Ho, L. C. 2014, Nature, 513, 210

Shen, Y., & Liu, X. 2012, ApJ, 753, 125

Shen, Y., Richards, G. T., Strauss, M. A., et al. 2011, ApJS, 194, 45

Shin, J., Nagao, T., Woo, J.-H., & Le, H. A. N. 2019, ApJ, 874, 22

Shin, J., Woo, J.-H., Nagao, T., Kim, M., & Bahk, H. 2021, ApJ, 917, 107

Steffen, A. T., Strateva, I., Brandt, W. N., et al. 2006, AJ, 131, 2826

Sulentic, J. W., Zwitter, T., Marziani, P., & Dultzin-Hacyan, D. 2000, ApJ, 536, L5

Sunyaev, R., & Titarchuk, L. 1980, A&A, 86, 121

Taylor, M. B. 2005, Astron. Data Anal. Soft. Syst. XIV, 347, 29

Temple, M. J., Ferland, G. J., Rankine, A. L., et al. 2020, MNRAS, 496, 2565

Temple, M. J., Ferland, G. J., Rankine, A. L., Chatzikos, M., & Hewett, P. C. 2021, MNRAS, 505, 3247

Temple, M. J., Matthews, J. H., Hewett, P. C., et al. 2023, MNRAS, 523, 646

Thompson, K. L., Hill, G. J., & Elston, R. 1999, ApJ, 515, 487

Timlin, J. D., Brandt, W. N., Ni, Q., et al. 2020, MNRAS, 492, 719

Trakhtenbrot, B., Ricci, C., Koss, M. J., et al. 2017, MNRAS, 470, 800

Tsuzuki, Y., Kawara, K., Yoshii, Y., et al. 2006, ApJ, 650, 57

Ueda, Y., Hashimoto, Y., Ichikawa, K., et al. 2015, ApJ, 815, 1

Uomoto, A., Wills, B., & Wills, D. 1976, AJ, 81, 905

Vanden Berk, D. E., et al. 2001, AJ, 122, 549

Verner, E., Bruhweiler, F., Verner, D., Johansson, S., & Gull, T. 2003, ApJ, 592, L59

Vestergaard, M., & Peterson, B. M. 2006, ApJ, 641, 689

Vestergaard, M., & Wilkes, B. J. 2001, ApJS, 134, 1

Vietri, G., Piconcelli, E., Bischetti, M., et al. 2018, A&A, 617, A81

Vignali, C., Brandt, W. N., & Schneider, D. P. 2003, AJ, 125, 433

Wang, J.-M., Du, P., Hu, C., et al. 2014, ApJ, 793, 108

Wang, C., Luo, B., Brandt, W. N., et al. 2022, ApJ, 936, 95

Wilhite, B. C., Brunner, R. J., Grier, C. J., Schneider, D. P., & Vanden Berk, D. E. 2008, MNRAS, 383, 1232

Wu, Q., & Shen, Y. 2022, ApJS, 263, 42

Yang, J., Wang, F., Fan, X., et al. 2020, ApJ, 897, L14

Zamfir, S., Sulentic, J., Marziani, P., & Dultzin, D. 2010, MNRAS, 403, 1759

Zappacosta, L., Piconcelli, E., Giustini, M., et al. 2020, A&A, 635, L5

Zubovas, K., & King, A. 2013, ApJ, 769, 51

Appendix A: LBT spectra atlas

Figure A1 shows all the LBT *zJ* spectra along with their uncertainty and the best-fit model components. The red dashed line is the best-fit model. The blue line is the continuum power law, where the blue square marks the 2500 Å luminosity density. The grey line represents the Fe II_{UV} pseudo-continuum, while the magenta emission line, if present, denotes the Mg II emission

feature. The grey shaded areas were excluded from the fit. Figure A2 shows all the LBT K_S spectra. The colour-coding is the same as in Figure A1 for the best-fit model, continuum (in this case the blue square represents the 5100 Å flux), and iron (Fe II_{opt}). The green emission lines represent the narrow and broad Hβ components, while the [O III] is shown in orange. Luminosities were calculated assuming a standard concordance cosmology with $H_0 = 70$ km s^{-1} Mpc^{-1}, $\Omega_0 = 0.3$, and $\Omega_\Lambda = 0.7$.
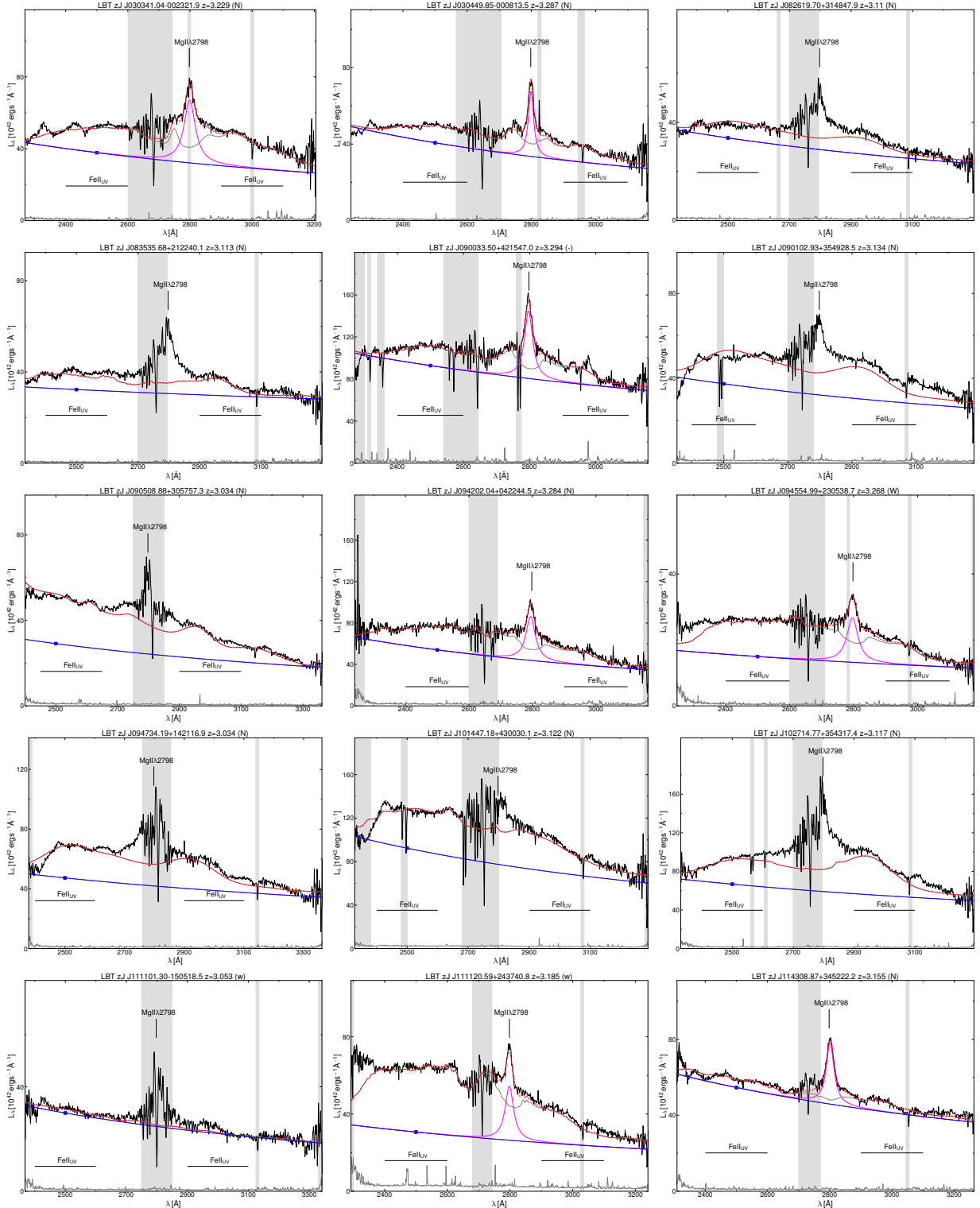

Fig. A.1. LBT *zJ* spectra. The colour-coding is described in Appendix B.
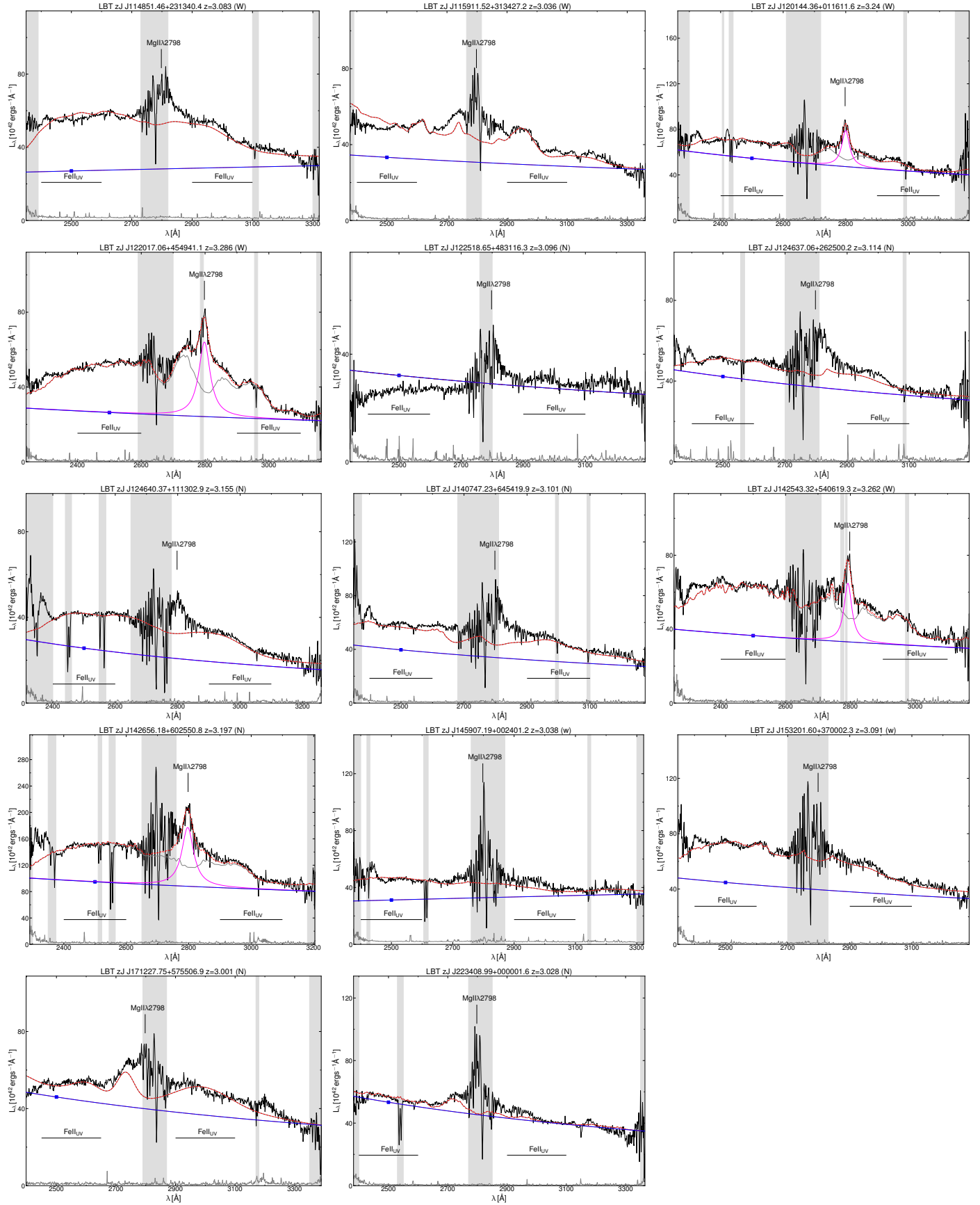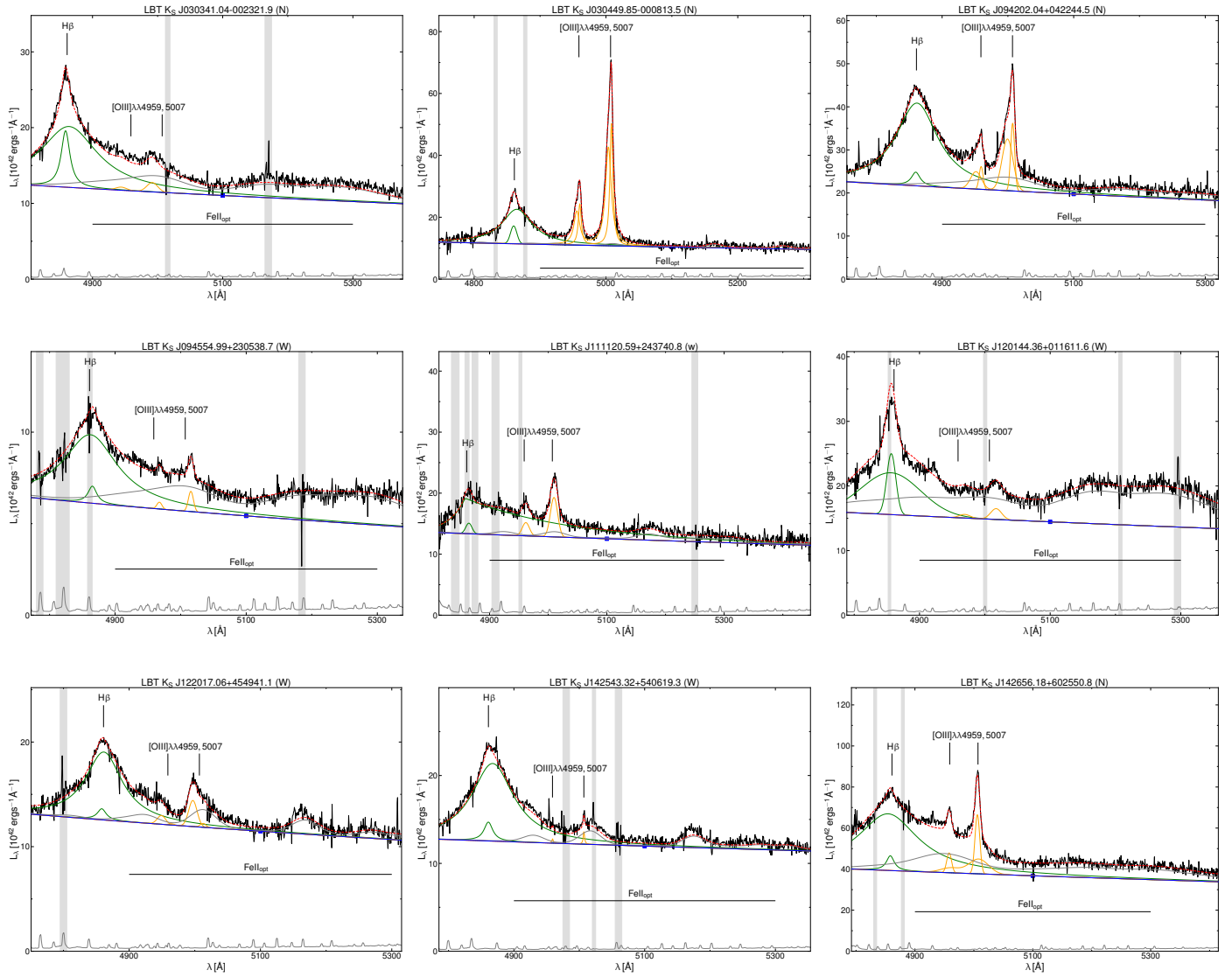
Fig. A.1. continued.

Fig. A.2. LBT K_S spectra. The colour-coding is described in Appendix B.

Table A.1. UV spectral properties of the $z \sim 3$ sample.

Name	X-ray class	EW Mg II [Å]	EW Fe II$_{UV}$ [Å]	Fe II/Mg II	EW Hβ [Å]	EW [O III] [Å]	EW Fe II$_{opt}{}^{a}$ [Å]
J0301-0035	N	82.8±9.5	373.4±36.9	4.5±0.5	109.9±4.1	2.3±0.2	53.6±2.5
J0304-0008	N	35.3±2.6	196.7±49.7	5.6±1.0	77.2±2.5	77.0±2.1	7.3±5.8
J0826+3148	N	-	127.6±74.8	-	-	-	-
J0835+2122	N	-	135.6±8.6	-	-	-	-
J0900+4215	-	40.9±0.8	131.9±14.6	3.2±0.3	-	-	-
J0901+3549	N	-	299.7±87.2	-	-	-	-
J0905+3057	N	-	695.5±144.9	-	-	-	-
J0942+0422	N	62.0±2.1	315.0±14.2	5.1±0.5	108.0±3.7	18.1±3.1	32.1±8.4
J0945+2305	W	72.4±4.0	511.9±70.2	7.1±1.5	95.5±8.9	1.9±0.3	77.4±7.5
J0947+1421	N	-	312.2±150.5	-	-	-	-
J1014+4300	N	-	318.3±21.0	-	-	-	-
J1027+3543	N	-	341.6±48.1	-	-	-	-
J1111-1505	w	-	32.2 ±2.9	-	-	-	-
J1111+2437	w	59.2±14.3	801.3±70.1	13.5±7.4	81.4±41.1	7.8±0.6	13.3±2.0
J1143+3452	N	36.5±0.5	77.2 ±11.8	2.1±0.3	-	-	-
J1148+2313	W	-	650.4±123.9	-	-	-	-
J1159+3134	W	-	547.4±49.6	-	-	-	-
J1201+0116	W	34.3±1.7	178.7±8.3	5.2±0.5	47.0±8.6	2.4±1.0	96.6±13.8
J1220+4549	W	118.5±12.7	679.3±31.3	5.7±1.1	55.1±1.1	3.7±0.3	20.0±1.5
J1225+4831	N	-	-	-	-	-	-
J1246+2625	N	-	151.1±30.5	-	-	-	-
J1246+1113	N	-	584.3±183.6	-	-	-	-
J1407+6454	N	-	394.6±104.6	-	-	-	-
J1425+5406	W	46.4±2.8	486.4±52.2	10.5±1.2	85.8±1.4	0.5±0.6	17.7±1.3
J1426+6025	N	76.7±5.5	364.5±56.8	4.8±0.6	136.6±55.3	15.9±2.6	51.2±25.5
J1459+0024	w	-	324.7±25.7	-	-	-	-
J1532+3700	w	-	472.5±102.9	-	-	-	-
J1712+5755	N	-	222.1±17.3	-	-	-	-
J2234+0000	N	-	54.0 ±0.5	-	-	-	-

Notes. ^{a}EW Fe II$_{opt}$ evaluated between 4900–5300 Å.

Table A.1. continued.

FWHM Mg II [km s^{-1}]	FWHM Hβ [km s^{-1}]	L$_{\text{[O III]}\lambda5007}$ [10^{42} erg s^{-1}]	Log L$_{3000\text{Å}}$ [erg s^{-1}]	Log L$_{5100\text{Å}}$ [erg s^{-1}]	Log M$_{\text{BH}}$ [M$_\odot$]	λ_{Edd}	α_{OX}	$\Delta\alpha_{\text{OX}}$	Γ
4693±25	6509±134	25.8±2.3	46.94	46.75	9.8±0.2	0.8	-1.68	0.02	$1.87^{+0.08}_{-0.07}$
2105±15	3946±180	839.0±13.4	46.95	46.73	9.2±0.2	4.6	-1.64	0.07	$1.99^{+0.05}_{-0.06}$
-	-	-	46.90	-	9.7±0.4	0.7	-1.87	-0.17	$1.56^{+0.17}_{-0.16}$
-	-	-	46.95	-	9.8±0.4	0.4	-1.67	0.03	$1.77^{+0.07}_{-0.06}$
3214±34	-	-	47.34	-	9.9±0.2	1.0	-1.56	0.20	$1.83^{+0.03}_{-0.03}$
-	-	-	46.94	-	9.7±0.4	0.9	-1.82	-0.12	$1.60^{+0.07}_{-0.08}$
-	-	-	46.81	-	9.1±0.4	4.0	-1.60	0.11	$2.12^{+0.06}_{-0.05}$
3830±52	4779±75	369.5±64.9	47.06	47.00	9.6±0.2	1.2	-1.70	0.02	$2.11^{+0.11}_{-0.10}$
4487±39	6156±223	10.7±1.5	46.56	46.44	9.7±0.2	0.1	-1.97	-0.3	1.80(f)
-	-	-	47.07	-	10.0±0.4	0.5	-1.71	0.03	$1.88^{+0.06}_{-0.05}$
-	-	-	47.32	-	10.0±0.4	1.1	-1.83	-0.05	$2.21^{+0.08}_{-0.09}$
-	-	-	47.22	-	10.0±0.4	0.9	-1.71	0.05	$1.91^{+0.06}_{-0.05}$
-	-	-	46.82	-	10.0±0.4	0.3	-1.88	-0.20	$1.71^{+0.13}_{-0.13}$
3481±150	8187>	99.5±4.7	46.86	46.81	9.6±0.2	1.2	-1.91	-0.19	$1.77^{+0.13}_{-0.12}$
3177±39	-	-	47.09	-	9.7±0.2	1.4	-1.68	0.04	$1.94^{+0.06}_{-0.05}$
-	-	-	46.94	-	10.0±0.4	0.3	-2.12	-0.35	$1.16^{+0.11}_{-0.11}$
-	-	-	46.94	-	10.1±0.4	0.3	-2.14	-0.42	1.8(f)
3208±27	6530±177	35.3±15.2	47.11	46.86	9.7±0.2	1.0	-2.00	-0.30	$1.60^{+0.14}_{-0.14}$
4646±30	4183±117	44.1±3.9	46.84	46.77	9.5±0.2	0.4	-2.04	-0.34	$1.70^{+0.31}_{-0.28}$
-	-	-	46.91	-	9.9±0.4	0.4	-1.59	0.12	$1.89^{+0.05}_{-0.04}$
-	-	-	47.01	-	10.4±0.4	0.2	-1.75	-0.04	$2.00^{+0.07}_{-0.07}$
-	-	-	46.74	-	9.6±0.4	0.9	-1.70	-0.02	$2.14^{+0.31}_{-0.28}$
-	-	-	46.97	-	9.9±0.4	0.8	-1.71	0.02	$2.07^{+0.08}_{-0.07}$
3110±15	4778±70	5.5±7.2	46.97	46.79	9.5±0.2	0.9	-1.99	-0.28	1.80(f)
4932±52	7645±275	597.8±102.2	47.40	47.27	10.1±0.2	1.1	-1.74	0.04	$1.81^{+0.05}_{-0.04}$
-	-	-	47.01	-	9.6±0.4	0.3	-1.91	-0.20	$1.72^{+0.27}_{-0.24}$
-	-	-	47.04	-	10.1±0.5	0.4	-1.92	-0.18	$1.69^{+0.11}_{-0.11}$
-	-	-	47.04	-	9.0±0.4	4.7	-1.62	0.09	$1.68^{+0.04}_{-0.05}$
-	-	-	47.09	-	9.0±0.4	5.0	-1.68	0.05	$1.86^{+0.05}_{-0.05}$

Appendix B: Optical and UV properties of the z = 3.0–3.3 sample

Table A1 contains the quantities evaluated from the LBT *zJ* and K_S spectra relevant for the topics discussed throughout the paper.

Appendix C: Possible systematics on Fe II emission, and a consistency check

It is important to explore, at least qualitatively, the possible systematic differences on the estimate of the Fe II$_{UV}$ emission with other samples in literature. First, we must take into account that most results are obtained using an iron emission template (Vestergaard & Wilkes 2001; Tsuzuki et al. 2006) or some modified version of it, whereas ours are computed as the emission of several synthetic BLRs with different ionisation parameters. Different fitting approaches may also affect the results. Fixing the spectral slope provides a decent baseline to the iron emission in the majority of the cases, but the modelling of the overall emission is not always optimal, and in one case (J1111+2437) the slope is likely too flat to adequately reproduce the data. A detailed study of how these systematics can affect the results can also be found in Section 5.3 of Shin et al. (2019).

Ideally, we would need a larger spectral range to fit the continuum, pivoting on two (or more) continuum windows and covering the interval 2200–3090 Å, in order to have both a more robust determination of the continuum and a direct estimate of the whole Fe II emission without relying on extrapolations at shorter wavelengths. Whilst the first of these two problems is present in our sample, the second should be a minor issue as the extrapolation on the blue side is generally limited to an interval ~100 Å wide, with the bulk of the iron emission covered by the observations. Although the issues mentioned above could affect a fair comparison with the other literature samples, the difference between the average values for the *N* and the *W+w* groups should not be influenced by these possible systematics, as both the *N* and the *W+w* average would eventually be affected in the same way.

We performed a consistency check of our capability to reproduce the iron emission. We selected a sample of 100 quasars present in the SDSS DR17 catalogue whose spectra had already been analysed in Wu & Shen (2022), and we performed the fit again, focusing on a reliable reproduction of the iron pseudo-continuum. To this end, we applied some filters in order to build an ad hoc sample: since EW Fe II in the Wu & Shen (2022) catalogue is evaluated between 2250–2650 Å we required this wavelength interval to be fully present in all the spectra, together with the Mg II and the C IV emission lines and the nearby continuum windows for a robust estimate of the continuum. We also required that both the emission lines satisfied the quality cuts suggested by the authors (see their Table 2 and relative discussion in Section 4), namely $F_{line}/\sigma_{F_{line}} > 2$, $38 < \log(L_{line}/\mathrm{erg\,s^{-1}}) < 48$ and $N_{pix,line\,complex} > 0.5 \times N_{pix,line\,complex\,max}$, which sets the minimum fraction of available pixels for the fit. Moreover, we filtered out sources affected by BALs by imposing the BAL_PROB field equal to 0, since these features could hamper a proper determination of the continuum. Finally, we also required a detected iron emission by requiring FEII_UV_EW>0. We sorted out the sources according to their SNR_MEDIAN_ALL parameter, and selected 100 of the best-quality spectra, avoiding objects affected by bad pixels and spurious features. Successively, we performed a one-by-one analysis, fitting each of them, adopt-
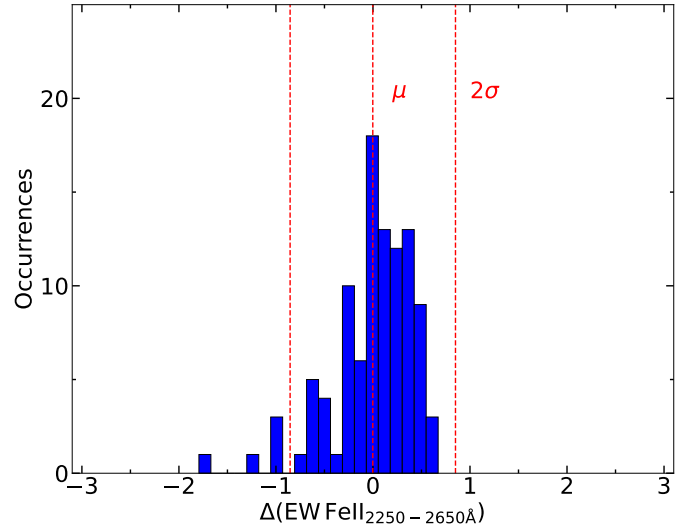
Fig. C.1. Distribution of residuals between our estimates of EW Fe II and catalogue values for an SDSS control sample.

ing the same double-Gaussian (1 broad, 1 narrow) deconvolution adopted in Wu & Shen (2022), but using two sets of our iron templates. After a careful visual inspection of the results, we estimated the EW Fe II for each object, and compared it against the catalogue values. The distribution of the relative differences between our estimates and the catalogue values ΔFe II=(EW Fe II$_{ours}$−EW Fe II$_{catalogue}$)/EW Fe II$_{catalogue}$ is illustrated in Figure C.1. The offset of the distribution is minimal, $\langle\Delta(\mathrm{Fe\,II})\rangle$=0.002, and most of the sample (95%) is consistent within a factor of ~2 with the catalogue estimates. Even in the case of strong iron emission both the continuum and the Fe II profile are well reproduced. This check led to some considerations. First, despite some scatter, in general there is not a strong systematic offset between our estimates and the reference values This points to the fact that using the region including the C IV line and its neighbouring continuum windows to estimate the continuum power law produces reliable results also in the Mg II region. Second, we could think of the dispersion of the residuals as a crude estimate of the uncertainty that we get when comparing our Fe II/Mg II estimates against those evaluated adopting other templates. Third, the good reproduction of the iron emission, even in the case of high EW Fe II, confirms that our analysis is capable of accurately sampling even the high-equivalent width tail of the EW Fe II distribution.

Appendix D: A check on [O III] extinction

We checked for the presence of dust extinction affecting the [O III] emission in X-ray weak quasars by applying increasing reddening to the [O III] emission of X-ray normal quasars. If the dearth of [O III] emission in *W+w* quasars were not intrinsic, but instead due to extinction, the average line profile of *N* quasars, once reddened, would be similar to the *W+w* profile. To rule out this possibility, we performed the following exercise: adopting the best fit model for the [O III] emission, we reddened the line profile with increasing values of $E(B-V)$ and evaluated at each step the EW of the line, checking whether this was compatible with the average EW [O III] for X-ray weak sources. To this end, we only considered the *N* quasars with average emission, excluding J0303−0023, whose [O III] is barely detectable, and J0304−0008 whose [O III] is the brightest. We
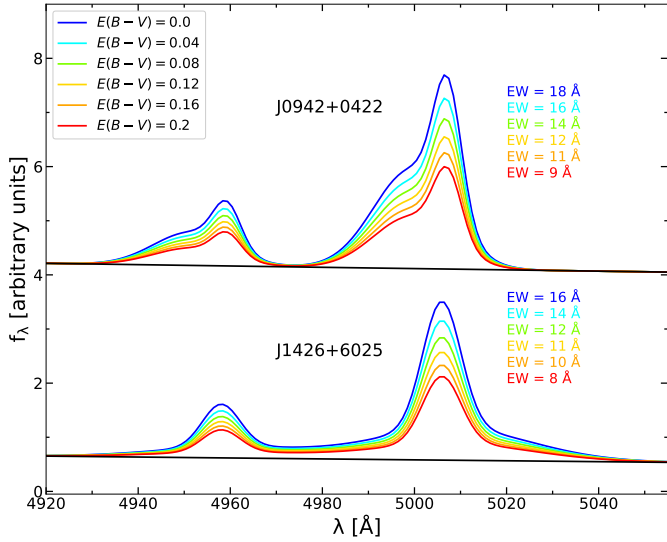
Fig. D.1. [O III] region of J0942+0422 and J1426+6025 reddened according to different $E(B-V)$ values (see colour-coding in legend). All the spectra are normalised by the $f_{5100Å}$ of the continuum. The spectra of J0942+0422 were shifted for visualisation purposes.

assumed the extinction curve from Gordon et al. (2016) available in the *dust_extinction* package of the Astropy software (Robitaille et al. 2013), adopting an absolute to selective extinction ratio $R_V = A_V/E(B-V) = 3.1$ and setting the parameter f_A equal to 0 (i.e. choosing a SMC-like extinction curve). We then corrected the rest frame 4900–5200 Å emission for increasing values of extinction $E(B-V)$ from 0 (unobscured) to 0.2 (reddened), which is twice the value adopted for the selection of blue continuum emission for a standard quasar SED (Richards et al. 2006), with steps of $\Delta E(B-V) = 0.02$. The results of this procedure are shown in Fig. D.1. Even in the case of significant reddening the [O III] profile is not suppressed to the level observed in the $W+w$ subsample, and the EW [O III] of the reddened spectra are still well above the median value for the X-ray weak sample (2.4 Å). We thus believe that the [O III] emission of X-ray weak quasars is unlikely to be affected by extinction.

Appendix E: Notes on individual objects

J0303−0023

This is the only X-ray normal object with faint [O III] emission. There are different scenarios that could justify such a weak line profile without invoking a significant difference in the ionizing SED (a list of possible explanations is examined in Sect. 4.2 of Agostino et al. 2023, and references therein). For instance, a low covering fraction of the NLR could obliterate the [O III] emission without altering the observed X-ray properties. Another possible reason for a weak [O III] profile in presence of normal X-ray emission is the case of NLR gas depletion, due to galactic activity (e.g. major mergers, gas stripping). In principle, for an individual object, it would be also important to consider the dif-

ference in size and characteristic timescales between the X-ray corona and the much farther region producing the [O III] emission. Although unlikely, since none of our sources deviate from the $L_X-L_{[O III]}$ relation, we cannot completely exclude that the AGN in J0303−0023 has experienced a sudden re-brightening to which the NLR has not yet been able to respond.

J0942+0422

This source presents a broad (FWHM=1173±27 km s^{-1}) blueshifted (v_{off}=469±17 km s^{-1}) component in the [O III] profile. The width and offset velocity are compatible with a galactic scale outflow. However, because this source an X-ray normal quasar, this feature does not relate with any exotic X-ray behaviour.

J1111+2437

The Hβ found in the optical spectrum of this object does not show a clear line profile and was thus fitted adopting a broken power-law profile convolved with a Gaussian kernel. The resulting shape is very skewed with a red side that extends well below the [O III] doublet. In this case the derived FWHM of the Hβ profile is considered an upper limit rather than a proper estimate.

J1148+2313

A visual inspection of the spectrum suggests that the slope of the continuum power law may be inverted with respect to that fitting the SDSS data, and this is confirmed if we try to fit the spectrum without fixing the slope. This leads to a higher value of EW [Fe II] than we would find by allowing the slope to vary. However, because the Mg II emission of this object is affected by atmospheric extinction, it is not included in the sample used to evaluate the Fe II/Mg II ratio, and does not alter the subsequent results.

J1225+4831

The slope derived on the blue SDSS side of the spectrum of this object is not able to reproduce the shape of the LBT zJ counterpart. Even adopting a free slope to fit this spectrum, the result is modest as we are not able to include any iron emission, and we thus exclude this object from the considerations in which such a feature is implied.

J1426+6025

The optical spectrum of this object shows a bump redwards the Hβ line, partially embedding the [O III] $\lambda4959Å$ emission. We interpreted this emission as produced by optical Fe, as it seems unlikely that Hβ could display such a broad redshifted component. At the same time, we cannot completely rule out the presence of intense blueshifted [O III] wings, as the resulting profile is degenerate for the combination of such wings and the Fe$_{opt}$ emission.